

# Non-Equilibrium ionisation and cooling of metal-enriched gas in the presence of a photo-ionisation background

Benjamin D. Oppenheimer<sup>1,2</sup>, Joop Schaye<sup>1</sup>

<sup>1</sup> *Leiden Observatory, Leiden University, PO Box 9513, 2300 RA Leiden, the Netherlands*

<sup>2</sup> *CASA, Department of Astrophysical and Planetary Sciences, University of Colorado, Boulder, CO 80309, USA*

20 September 2018

## ABSTRACT

Simulations of the formation of galaxies, as well as ionisation models used to interpret observations of quasar absorption lines, generally either assume ionisation equilibrium or ignore the presence of the extra-galactic background (EGB) radiation. We introduce a method to compute the non-equilibrium ionisation and cooling of diffuse gas exposed to the EGB. Our method iterates the ionisation states of the 11 elements that dominate the cooling (H, He, C, N, O, Ne, Si, Mg, S, Ca, & Fe) and uses tabulated ion-by-ion cooling and photo-heating efficiencies to update the temperature of the gas. Our reaction network includes radiative and di-electric recombination, collisional ionisation, photo-ionisation, Auger ionisation, and charge transfer. We verify that our method reproduces published results for collisional equilibrium, collisional non-equilibrium, and photo-ionised equilibrium. Non-equilibrium effects can become very important in cooling gas, particularly below  $10^6$  K. Photo-ionisation and non-equilibrium effects both tend to boost the degree of ionisation and to reduce cooling efficiencies. The effect of the EGB is larger for lower densities (i.e. higher ionisation parameters). Hence, photo-ionisation affects (equilibrium and non-equilibrium) cooling more under isochoric than under isobaric conditions. Non-equilibrium effects are smaller in the presence of the EGB and are thus overestimated when using collisional-only processes. The inclusion of the EGB alters the observational diagnostics of diffuse, metal-enriched gas (e.g. metal absorption lines probed in quasar sight lines) even more significantly than the cooling efficiencies. We argue that the cooling efficiency should be considered if ionisation models are used to infer physical conditions from observed line ratios, as the a priori probability of observing gas is lower if its cooling time is shorter. We provide on-line tables of ionisation fractions and cooling efficiencies, as well as other data, for equilibrium and non-equilibrium scenarios, and both with and without an EGB. Cooling efficiencies and diagnostics of the physical state of diffuse gas can become highly inaccurate if ionisation equilibrium is assumed or if the existence of the ionising background is ignored.

**Key words:** atomic processes; plasmas; galaxies: formation; intergalactic medium; quasars: absorption lines; cosmology: theory;

## 1 INTRODUCTION

The rates at which diffuse gases cool radiatively are central to numerous baryonic processes in astrophysics. In the context of galaxy formation, how gas cools in the intergalactic medium (IGM) and galactic haloes critically determines if, how, and when galaxies receive their gas, which provides the main source of fuel for star formation.

The ejection of the nucleosynthetic products of star formation (metal species) into diffuse regions complicates the picture, as these sub-dominant heavier atomic species

are very efficient coolants, owing to their more numerous electrons and line transitions. The inclusion of radiative metal cooling in gas enriched to solar metal abundances ( $Z_{\odot}$ ) or even  $0.1 Z_{\odot}$  significantly reduces cooling times and directly leads to more efficient accretion onto galaxies (e.g. Oppenheimer & Davé 2006; Choi & Nagamine 2009; Schaye et al. 2010; van de Voort et al. 2012; Haas et al. 2012).

Diffuse regions outside of galaxies are photo-ionised and photo-heated by the extra-galactic background (EGB) originating from a combination of UV and X-ray emitting

sources including active galactic nuclei (AGN) and star-forming galaxies (e.g. Haardt & Madau 1996, 2012). Photo-ionisation of hydrogen, helium, and metal species reduces cooling efficiencies, because fewer bound electrons provide fewer line transitions for radiative cooling (Efstathiou 1992; Wiersma et al. 2009a, hereafter W09). W09 showed net cooling efficiencies declined by an order of magnitude at typical densities and temperatures of the shock-heated IGM. Including the effect of photo-ionisation on metal cooling efficiencies can therefore significantly affect the appearance of metal absorption in quasar absorption line (QAL) spectra (Tepper-Garcia et al. 2011; Oppenheimer et al. 2012) and alter the dynamics of the accreting gas onto galaxies (Smith et al. 2011; Oppenheimer et al. 2012).

Most hydrodynamic simulations and semi-analytic models assume that gas is in ionisation equilibrium, but this assumption can break down if the ionisation or recombination time of a species is long compared to other timescales, including the dynamical, Hubble, or cooling timescales. For example, Gnat & Sternberg (2007, hereafter GS07) calculated that when the timescale of recombination exceeded that for cooling, a “recombination lag” occurs where the gas is over-ionised relative to the equilibrium case (e.g. Kafatos 1973; Shapiro & Moore 1976; Schmutzler & Tscharnuter 1993; Sutherland & Dopita 1993; Cen & Fang 2006; Yoshikawa & Sasaki 2006; Vasiliev 2013). By following the ionisation state of gas without any external radiation (i.e. collisional processes only), they find fewer bound electrons for metal ion species with long recombination times and that this results in less efficient net cooling and cooling functions of temperature with less sharp peaks.

Vasiliev (2011) calculated non-equilibrium ionisation and cooling rates in the presence of a UV/X-ray radiation field, including the Haardt & Madau (2001) field and power-law spectra corresponding to AGN and stellar clusters. He demonstrated that photo-ionisation suppressed cooling by ionising metals to higher states, which combined with the recombination lag, made photo-ionised non-equilibrium cooling less efficient than the collisional-only non-equilibrium cases of GS07.

In this paper, we develop a new method to follow non-equilibrium ionisation and cooling in the presence of a photo-ionising EGB, focusing on temperatures  $\geq 10^4$  K. By self-consistently tracking the ionisation state of primordial and metal species, we can accurately calculate the non-equilibrium cooling rates of metal-enriched gas. In §2, we introduce and test the method that we have integrated into the GADGET-3 (last described in Springel 2005) hydrodynamical simulations code for hydrogen, helium, electrons, and the important metal coolants (carbon, nitrogen, oxygen, neon, magnesium, silicon, sulphur, calcium, and iron). To demonstrate the effects and importance of non-equilibrium processes, we use a stand-alone, “single-particle” version of the code to follow the ionisation and temperature evolution of a parcel of gas independent of any hydrodynamics, but still in the presence of an EGB. We diagnose how non-equilibrium effects diverge from the equilibrium case for enriched cooling gases without photo-ionisation in §3 and with photo-ionisation in §4. Relevant astrophysical applications include metal-enriched materials ejected into the IGM and the circumgalactic medium by superwinds, which simula-

tions show regularly re-accrete onto galaxies at late times ( $z \lesssim 1$ ; Oppenheimer et al. 2010; van de Voort et al. 2012). We show that the combination of non-equilibrium effects and photo-ionisation can retard accretion and significantly alter the observational diagnostics of cooling gas that may be observed via metal-line absorption with instruments such as the Cosmic Origins Spectrograph (COS) on the *Hubble Space Telescope*. Finally, we summarise our findings in §5.

We provide on-line tables including cooling and photo-heating efficiencies per ion, ionisation fractions in equilibrium and non-equilibrium cases, and the compiled atomic data used in this work at <http://noneq.strw.leidenuniv.nl>. Supplementary figures are also available at this website.

## 2 METHOD AND TESTS

Our method explicitly follows the ionisation states of all 11 elements that contribute significantly to the cooling efficiencies at temperatures  $T \geq 10^4$  K (i.e. H, He, C, N, O, Ne, Si, Mg, S, Ca, & Fe; W09) as well as the electron density. These are all the species tabulated by W09 and used in the Overwhelmingly Large Simulations (OWLS) project (Schaye et al. 2010). They account for nearly all the radiative cooling (W09; Bertone et al. 2013). Our method is meant to be complimentary to W09, so that we can turn off following the non-equilibrium ionisation states of any metal species and instead use the corresponding equilibrium tables. For example, iron involves following 27 ionic species, which may exacerbate the memory requirements when running a large simulation. The code can be used to follow only the metal-line coolants that dominate at a given temperature (C, O, Ne, & Fe), or it can be used to follow the ionisation states of species frequently detected in QAL observations (e.g. C, O, Si, & Mg). Species including S and Ca, which have many ions but are not very important for cooling and rarely seen in QAL spectra may be less useful to follow, so they can be turned off. We also build in options to turn off Auger ionisation and charge transfer reactions, because these calculations can significantly increase computation time in exchange for mostly minor changes in the ionisation balance.

Having computed the ionisation states for each species, we can use ion-by-ion lookup tables as functions of temperature and redshift for the cooling and photo-heating efficiencies. Because we explicitly track ionisation states, the lookup tables are much more compact than those of W09, who had to track net cooling efficiencies as a function of density, temperature, redshift, and helium fraction. Finally, we consider criteria to cycle and sub-cycle the time integration of ionisation and cooling.

Throughout, we will assume the gas to be optically thin to both the EGB and the cooling radiation. Assuming the gas to be optically thin is generally a good approximation for gas with densities  $n_{\text{H}} \lesssim 10^{-3} \text{ cm}^{-3}$  (Rahmati et al. 2012), but we note that for higher densities self-shielding may reduce the effects of photo-ionisation. We will ignore sources of ionising radiation other than the EGB, including self-radiation from shocks and local sources, which is a conservative assumption when investigating the potential effects of photo-ionisation. We will also assume that the electron and ion temperatures are equal. Although the electron temperature

may temporarily lag that of the ions in shock-heated gas, supernova remnants suggest that plasma waves quickly equilibrate the different temperatures (e.g. Bertone et al. 2008, and references therein).

We first discuss the method and tests of following the ionisation of the gas, then the cooling and photo-heating method and tests, and finally how we cycle and subcycle during timesteps.

## 2.1 Ionisation

We consider the processes of radiative and di-electric recombination, collisional ionisation, photo-ionisation by an EGB, Auger ionisation, and charge transfer in our calculations of the ionisation balance. For an ionisation state  $i$  of element  $x$ , the time dependent evolution (omitting Auger ionisation and charge transfer for simplicity) of the number density,  $n$ , of each ion species,  $x_i$ , is given by

$$\frac{dn_{x_i}}{dt} = n_{x_{i+1}}\alpha_{x_{i+1}}n_e + n_{x_{i-1}}(\beta_{x_{i-1}}n_e + \Gamma_{x_{i-1}}) - n_{x_i}((\alpha_{x_i} + \beta_{x_i})n_e + \Gamma_{x_i}), \quad (1)$$

where  $n_e$  is the free electron density ( $\text{cm}^{-3}$ ),  $\alpha_{x_i}$  is the total recombination rate coefficient (radiative plus dielectronic,  $\text{cm}^3 \text{s}^{-1}$ ),  $\beta_{x_i}$  is the collisional ionisation rate coefficient ( $\text{cm}^3 \text{s}^{-1}$ ), and  $\Gamma_{x_i}$  is the photo-ionisation rate ( $\text{s}^{-1}$ ) for the given ionisation state, where

$$\Gamma_{x_i} = \int_{\nu_{0,x_i}}^{\infty} \frac{4\pi J_\nu}{h\nu} \sigma_{x_i}(\nu) d\nu, \quad (2)$$

where  $\nu$  is frequency,  $\nu_{0,x_i}$  is the ionisation frequency,  $J_\nu$  is the EGB radiation field ( $\text{erg s}^{-1} \text{cm}^{-2} \text{Hz}^{-1} \text{sr}^{-1}$ ),  $\sigma_{x_i}(\nu)$  is photo-ionisation cross-section, and  $h$  is the Planck constant.

We use atomic data similar to that used by CLOUDY ver. 10.00<sup>1</sup> (last described in Ferland et al. 1998) where reasonably possible. For radiative and dielectronic recombination coefficients, we use the Badnell (2006) and Badnell et al. (2003) fits, respectively, if available for our species. Otherwise, we use the Verner & Ferland (1996) fits for radiative recombination if available, and finally recombination data compiled by D. Verner<sup>2</sup> from Aldrovandi & Pequignot (1973); Shull & van Steenberg (1982); Arnaud & Rothenflug (1985). We assume case A recombination. Fits to collisional ionisation rate coefficients are from Voronov (1997). We tabulate these coefficients between  $\log[T \text{ (K)}] = 2.0 - 9.0$  at 0.04 dex intervals resulting in 176 temperature bins, which is the same spacing as used by W09.

We perform the integral in Equation 2 using the same  $\sigma_{x_i}(\nu)$  as used in CLOUDY ver. 10.00 (Verner & Yakovlev 1995; Verner et al. 1996) for the appropriate EGB. In this work, we use the Haardt & Madau (2001, hereafter HM01) EGB as our fiducial background since this results in good agreement with the observed column density distribution of H I (Davé et al. 2010; Altay et al. 2011) and metal-line ratios (Aguirre et al. 2008). This EGB includes contributions

from quasars and galaxies and is tabulated at 50 redshifts between  $z = 0 - 9$  sampling at constant  $\log(1+z)$  intervals, resulting in a lookup table of  $\Gamma_{x_i}$ s as a function of redshift corresponding to each ion containing electrons. We also tabulate photo-ionisation rates for the Faucher-Giguère et al. (2009) and Haardt & Madau (2012) and make these available on our website.

Auger ionisation involves the ejection of multiple electrons following the ionisation of an inner shell electron. The Auger reaction is stimulated by an energetic photon,  $\gamma$ , such that when element A, initially ionised to charge  $+n$ , interacts with  $\gamma$ ,  $m$  electrons are released. The rate equation is then  $A^{+n} + \gamma \rightarrow A^{+n+m} + m e^-$ , where  $m > 1$ . We use the electron vacancy distribution probabilities calculated by Kaastra & Mewe (1993), and re-tabulated for CLOUDY as probabilities of ionising multiple numbers of electrons, all the way up to 10 electrons for the case of Fe I to Fe XI. Auger ionisation is significant for photo-ionised oxygen species, because 2 electron losses are common for inner shell ionisations of O I through O V. We include the option to turn Auger ionisation off, because it slows the calculation, or to lower  $m$  to values as low as two, if one does not want to follow the  $m > 2$  reactions that are mostly limited to heavier species like Fe.

Charge transfer reactions encompass two-body reactions where neutral H or He exchange an electron with a heavier ion species leading to recombination of the heavier ion. For hydrogen reacting with element A ionised to charge  $+n$ , the reaction is  $H^0 + A^{+n} \rightarrow H^+ + A^{+n-1}$ . The most significant reaction is the recombination of O II to O I owing to H I, which can enhance O I levels. The reverse reactions of singly ionised H and He with a heavier species ionises the heavier species such that for hydrogen,  $H^+ + A^{+n-1} \rightarrow H^0 + A^{+n}$ . CLOUDY uses rates from various references (e.g. Kingdon & Ferland 1996) to calculate the four varieties of charge transfer reactions: recombination and ionisation with H and He. We have outputted and tabulated these rates for our 176 temperatures from CLOUDY for all relevant metal ions with H and He, as well as charge transfer between H and He.

We use the Sundials CVODE<sup>3</sup> solver to integrate the ionisation states over a timestep  $dt$  to solve for each  $x_i$ . We use the backward difference formula (BDF) method and Newton iteration in CVODE, given the set of rate equations. For an atomic species with atomic number  $Z$ , there are  $Z + 1$  versions of Equation 1 to solve for the  $Z + 1$  ions that exist; hence the number of equations equals the number of unknowns. In practice we follow all  $Z + 1$  ions, even though an independent constraint is available, namely that the sum of all ion fractions equals one, which allows one to follow only  $Z$  states. We calculate  $\sum_i f_{x_i}$  for each element, where  $f_{x_i}$ s are ion fractions, as an independent check to see how well the BDF method is tracking the states, which depends on the accuracy that one chooses for the calculations using the relative and absolute tolerance parameters described in the CVODE manual. Briefly, for the calculations in this paper we set absolute tolerance vector to  $10^{-5} \times f_{x_i}$  for metal species and  $10^{-7} \times f_{x_i}$  for hydrogen and helium. The relative tolerances are  $10^{-5}$  and are unlikely to play a role,

<sup>1</sup> <http://www.nublado.org/>

<sup>2</sup> <http://www.pa.uky.edu/~verner/rec.html>

<sup>3</sup> <https://computation.llnl.gov/casc/sundials/main.html>

since the absolute tolerance vectors are equal or tighter, plus they act as relative tolerances since they are multiplied by the ionisation fraction. However, for the version integrated into GADGET-3, we will choose looser tolerances according to the computational resources. If  $\sum_i f_{x_i}$  strays more than 1% from unity, we renormalize the ionisation fractions. However, such deviations occur only in extreme situations and are especially rare given our low tolerances. Deviations from unity indicate that the timestep given to the CVODE solver is too large, which mostly affects the species with the most ions (e.g. Fe).

We combine all atomic species into one CVODE calculation, which includes  $Z + 1$  ions for each atomic species, as well as  $n_e$ , which we also follow in the solver. Including all eleven atomic species, we follow 134 rate equations. We include the option to turn off the rate equation for  $n_e$  if Auger ionisation and charge transfer are also turned off, because  $n_e$  depends on as many as 133 ions and ruins the symmetry of the Jacobian matrix (which Auger ionisation and charge transfer also break), causing the calculation to scale non-linearly with the number of rate equations. As most of the IGM is highly ionised and  $n_e$  changes very slowly outside of the H I and He II reionisation epochs, we build in the option to update  $n_e$  only after each CVODE iteration. For the calculations in this paper we follow everything self-consistently. Similarly, we leave Auger ionisation and charge transfer on in our calculations, but we generally recommend turning these off in a hydro simulation owing to longer computation times from non-symmetrical entries in the Jacobian.

### 2.1.1 Ionisation test cases

We demonstrate the capabilities of the ionisation solver by considering the evolution of initially neutral, solar abundance gas at a large range of densities and temperatures corresponding to diffuse gas regions. Figure 1 shows the ionisation state of oxygen in density-temperature phase space at five distinct times ( $t = 0.1$  Myr, 1 Myr, 10 Myr, 100 Myr, & 1 Gyr) after the neutral initial conditions, and also in equilibrium, which is nearly equivalent to the case after 10 Gyr.<sup>4</sup> In this example, we assume the  $z = 1$  HM01 EGB and neglect redshift evolution. We apply no cooling or photo-heating in this example, allowing us to focus on the ionisation behaviour by leaving the density and temperature constant. At  $t = 0$  (not shown), the entire phase space would be dark blue, corresponding to O I, while after 1 Myr, the highest densities and temperatures (regions that would typically be defined as the intracluster medium (ICM),  $n_H \gtrsim 10^{-3} \text{ cm}^{-3}$ ,  $T > 10^7$  K) have achieved complete ionisation to O IX, corresponding to dark red.

The evolution of the oxygen ionisation state over the next Gyr demonstrates how significant ionisation timescales lead to non-equilibrium ionisation behaviour. The ionisation timescale for a given ion  $i$  is

$$\tau_{\text{ion},x_i} = \frac{1}{\beta_{x_i} n_e + \Gamma_{x_i}}. \quad (3)$$

<sup>4</sup> For movies showing time evolution of the ionisation states, and also for other metal species, please visit <http://noneq.strw.leidenuniv.nl>.

The collisional ionisation timescale,  $\tau_{\text{coll},x_i} = 1/(\beta_{x_i} n_e)$ , depends inversely on density; hence the highest densities achieve equilibrium in less than a Myr. This includes gas collisionally ionised to O IX, which depends on eight ionisation timescales,  $\tau_{\text{ion},\text{O I}}$  through  $\tau_{\text{ion},\text{O VIII}}$ , all of which are  $\ll 1$  Myr at the highest densities shown in Figure 1. For each 1 dex increase in  $t$ , the density achieving collisional ionisation equilibrium (CIE), defined as where collisional ionisation exactly balances recombination, decreases by 1 dex. In CIE, the ionisation state depends only on  $T$ , which is why there is no density dependence at the highest densities where photo-ionisation by the uniform HM01 EGB is unimportant ( $\beta_{x_i} n_e \gg \Gamma_{x_i}$ ). In CIE the O VI fraction peaks at  $T \approx 10^{5.5}$  K, corresponding to the horizontal yellow band indicating this state on the right-hand side of each panel in Figure 1.

The photo-ionisation timescales,  $\tau_{\text{phot},x_i} = 1/\Gamma_{x_i}$ , are independent of density for a uniform EGB. At low densities where  $\tau_{\text{phot},x_i} \ll \tau_{\text{coll},x_i}$ , the ionisation state depends on the series of  $\tau_{\text{phot}}$ s, which increase with ionisation state. After 100 Myr the dominant ionisation state at low density ( $n_H \lesssim 10^{-6} \text{ cm}^{-3}$ ) is O VI and after 1 Gyr it is O VIII. The lowest densities, corresponding to the centres of voids at  $z = 1$  ( $n_H \lesssim 10^{-7} \text{ cm}^{-3}$ ), take nearly 10 Gyr (assuming the  $z = 1$  HM01 field) to achieve their equilibrium ionisation states, which are dominated by O IX for all temperatures.

The dashed vertical white line, indicates the density for which the dynamical timescale,

$$\tau_{\text{dyn}} = 1/\sqrt{G\rho}, \quad (4)$$

equals  $t$ , where  $G$  is the gravitational constant and  $\rho$  is the gas mass density.  $\tau_{\text{dyn}}$  is long compared to  $t$  to the left of this line. The line is beyond the right boundary of the  $\leq 10$  Myr panels, meaning that the gas exhibiting non-equilibrium ionisation states will, at these times, not be disrupted by dynamical processes. An astrophysically relevant case may be the injection of enriched, low-ionisation wind material into the IGM, where an ‘‘ionisation lag’’ leaves the gas under-ionised relative to equilibrium values. Cen & Fang (2006) found enriched gas was under-ionised in their cosmological simulation that explicitly followed the oxygen states O V – O IX, which was reflected in fewer predicted O VII and O VIII absorption line detections in their mock AGN X-ray spectra probing the IGM.

We provide a consistency check for the predicted ionisation fractions of our code by comparing to CLOUDY ver. 10.00 calculations in Figure 2 for gas in equilibrium, which we obtain for our code by integrating for at least  $100\times$  any recombination or ionisation timescale.

The top panel shows the equilibrium ionisation fractions for H I, C IV, O VI, and Ne VIII as a function of temperature for a density where collisional ionisation dominates,  $n_H = 0.1 \text{ cm}^{-3}$ . The dotted lines are from CLOUDY-generated ionisation lookup tables at  $z = 1$  assuming equilibrium. Our code produces the solid lines that reproduce the CLOUDY CIE behaviour of the four ions, which depend on the balance of recombination and collisional ionisation.

The bottom two panels of Figure 2 demonstrate the impact of photo-ionisation as a function of density for  $T = 10^4$  K (middle) and  $10^{5.5}$  K (bottom). Photo-ionisation dominates in the  $T = 10^4$  K case and the two codes agree well. For H I,  $n_{\text{HI}} \propto n_H$  because recombination ( $\propto n_e$ ) balances photo-ionisation (independent of  $n_e$ ) for this two-state species in

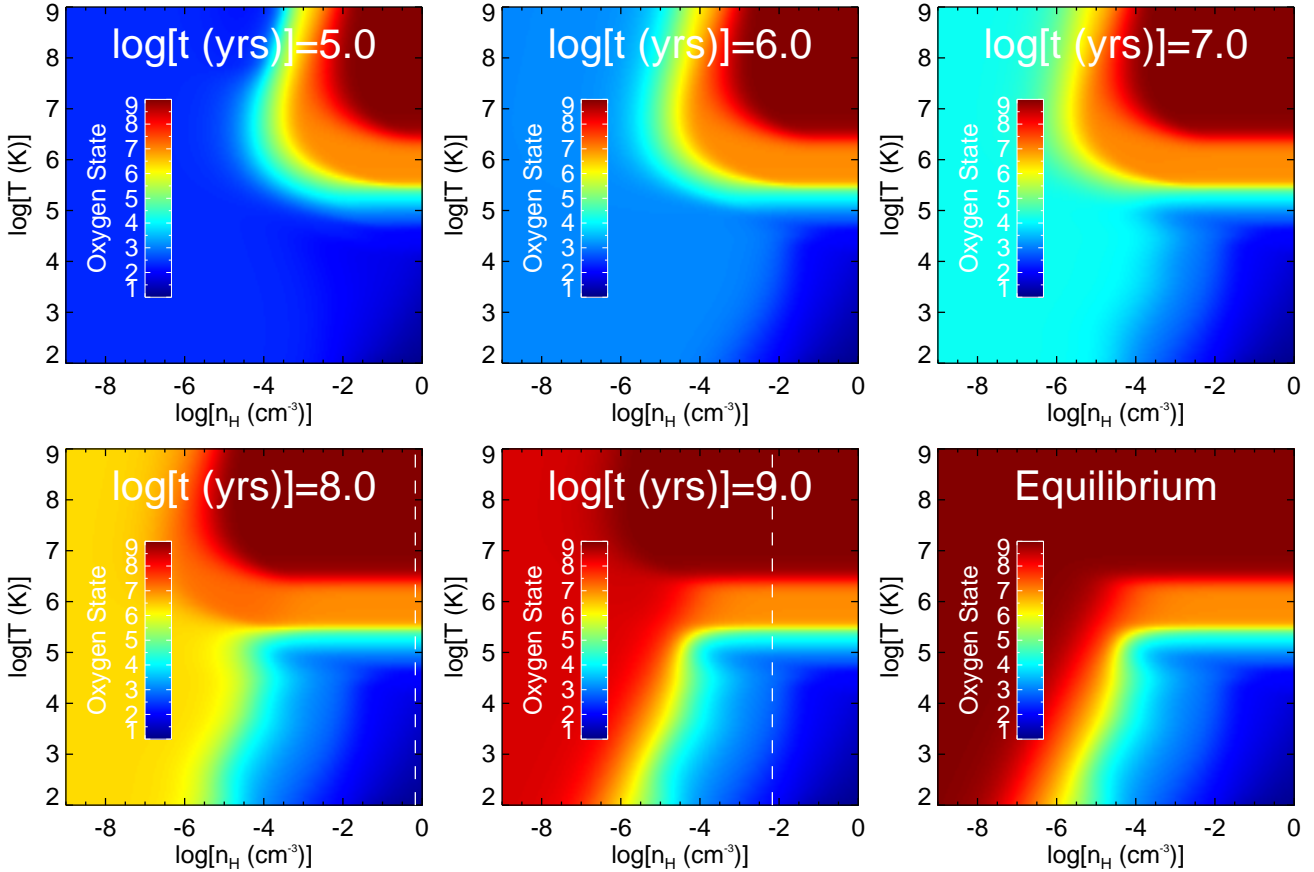


**Figure 1.** The evolution of non-equilibrium oxygen ionisation fractions starting from a neutral state at  $t = 0$  for a range of densities and temperatures using the  $z = 1$  HM01 radiation field. The colour indicates the average ionisation fraction, from O I (dark blue) to O IX (dark red). The first five panels correspond to the five distinct times indicated and the bottom right panel corresponds to the equilibrium case, which is reached by 10 Gyr for all densities. The vertical, dashed white line indicates where the dynamical time equals  $t$ , which only corresponds to densities in the displayed range at 100 Myr and 1 Gyr. This implies the area to the left of this line (the entire phase spaces at  $\leq 10$  Myr) would not be dynamically disrupted. Collisional ionisation timescales are shorter at high densities, achieving equilibrium values earlier. Photo-ionisation timescales are independent of density and equilibrium has not yet been achieved by 1 Gyr at the lowest densities where photo-ionisation dominates. For movies of the evolution, please visit <http://noneq.strw.leidenuniv.nl>.

equilibrium. In contrast, the lithium-like metal ions exhibit a peak ionisation fraction corresponding to a preferred density. As the atomic number increases, the energy required for ionisation increases, and the number of photons capable of ionising decreases for realistic spectra. Hence, the density at which the equilibrium ion fraction peaks declines with increasing atomic weight.

The  $T = 10^{5.5}$  K case shows that our code reproduces the transition from photo-ionisation to collisional ionisation at higher densities for all species. We choose this temperature specifically because O VI achieves its CIE peak at this temperature.  $f_{\text{HI}}$  asymptotes to  $10^{-6}$  in the collisional ionisation regime for this temperature. For further comparison tests between the equilibrium abundances predicted by our code and CLOUDY, we forward the reader to the Appendix and additionally our website—<http://noneq.strw.leidenuniv.nl>. We also demonstrate the effects of Auger ionisation and charge transfer in the Appendix. The examples in this Section have both of these processes turned on.

While these comparisons demonstrate that our reaction network contains all the important processes and that our

atomic data is close to that used by CLOUDY, they do not test the accuracy of time integration. We will test the time-dependent non-equilibrium behaviour in §3 when we compare the results of our method to GS07.

## 2.2 Radiative cooling and photo-heating

The net volumetric cooling rate ( $\Lambda_{\text{net}}$ ) is the difference between cooling and photo-heating rates. W09 tabulated net cooling tables under the assumption of ionisation equilibrium as functions of temperature, density, redshift, and helium fraction for 9 metals and primordial species separately. Here we make use of ion-by-ion cooling and photo-heating tables that are more compact and flexible, which can be combined into net cooling functions for both equilibrium and non-equilibrium calculations. Our ion-by-ion net cooling method uses the ion fraction calculated using the CVODE solver. We calculate net cooling as the difference between cooling rates ( $\Lambda'_{x_i} n_{x_i} n_e$ ) and photo-heating rates ( $\epsilon_{x_i} n_{x_i}$ ), where the resulting net cooling function for an ion  $x_i$  is

$$\Lambda_{\text{net}, x_i}(T, z, n_{x_i}, n_e) = \Lambda'_{x_i}(T) n_{x_i} n_e - \epsilon_{x_i}(z) n_{x_i} \quad (5)$$

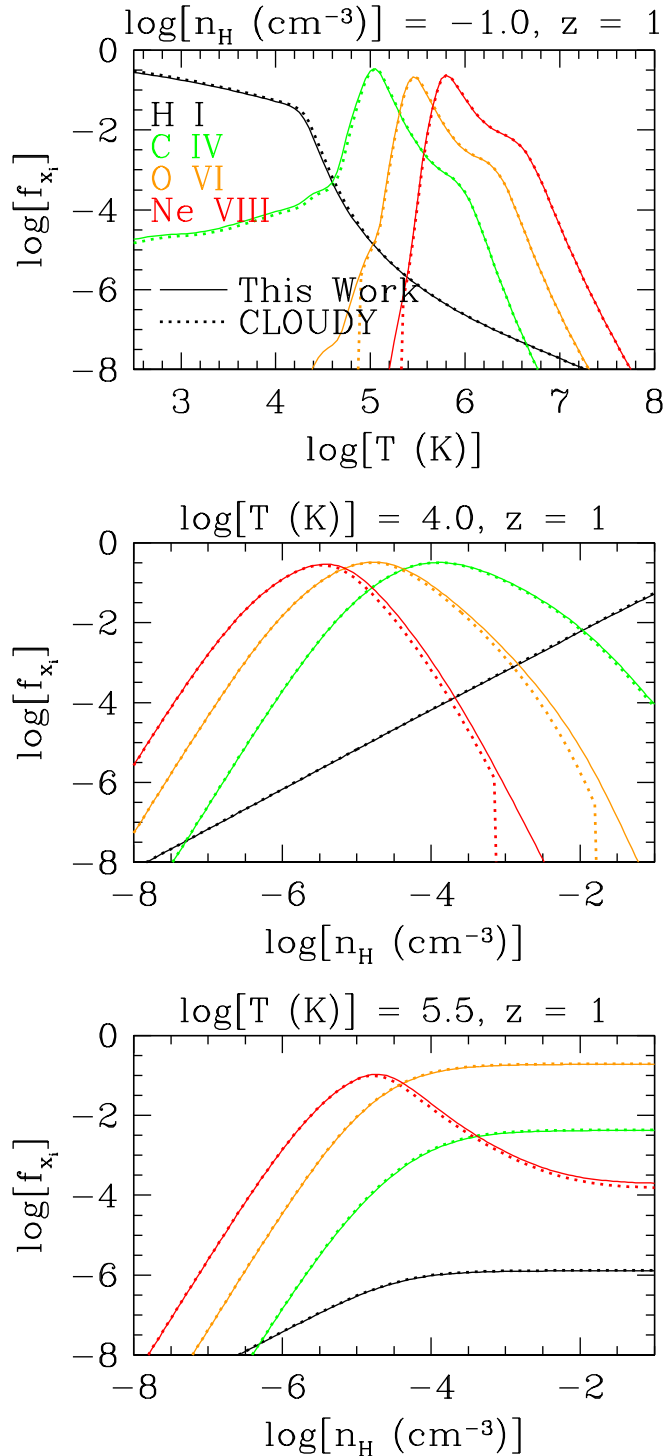


**Figure 2.** Comparisons of equilibrium ionisation fractions for H I, C IV, O VI, and Ne VIII predicted by our code and by CLOUDY using the  $z = 1$  HM01 radiation field. The top panel shows ion fractions as a function of temperature at the constant density  $n_{\text{H}} = 0.1 \text{ cm}^{-3}$ , for which collisional ionisation dominates in most species. The bottom two panels show ion fractions as a function of density at  $T = 10^{4.0}$  and  $10^{5.5}$  K, respectively. Photo-ionisation dominates the middle panel while the bottom panel tests the transition between the photo- and collisionally ionised regimes. The agreement with CLOUDY is excellent, although there is deviation at some very low metal ion fractions where CLOUDY does not accurately track these very low abundances.

The units of  $\Lambda'_{x_i}$ , ion-by-ion cooling efficiencies, are  $\text{erg cm}^3 \text{ s}^{-1}$  where we divide the volumetric cooling rate for an ion by  $n_{x_i} n_e$  to make  $\Lambda'$  independent of density (at least in the regime where electron-ion collisions dominate the cooling rate). Photo-heating is calculated in an analogous manner as photo-ionisation. The photo-heating efficiency for species  $x_i$  defined as

$$\epsilon_{x_i} = \int_{\nu_{0,x_i}}^{\infty} \frac{4\pi J_{\nu}}{h\nu} \sigma_{x_i}(\nu) h(\nu - \nu_{0,x_i}) d\nu, \quad (6)$$

and hence has unit  $\text{ergs s}^{-1}$ . We calculate  $\epsilon_{x_i}$  for our 133  $x_i$  species in units of  $\text{erg s}^{-1}$  for every ion given the HM01 EGB at the 50 redshifts between  $z = 0$  and 9, tabulating it in a table analogous to that of the photo-ionisation rates.

We have used our own method to calculate CLOUDY cooling efficiencies ion-by-ion ( $\Lambda'_{x_i}$ ), which was developed independently from Gnat & Ferland (2012), who also tabulate ion-by-ion cooling functions using the same version (ver. 10.00) of CLOUDY. We run CLOUDY to calculate individual ion cooling efficiencies at 176 temperature values between  $\log[T \text{ (K)}] = 2.0$  and 9.0. The end result is a set of cooling tables that include the effects of radiative and dielectronic recombination, collisional ionisation and excitation, and Bremsstrahlung. We have compared our ion cooling functions to those of Gnat & Ferland (2012) and find that our efficiencies are indistinguishable from theirs.<sup>5</sup>

In detail, we tabulate ion-by-ion cooling functions by running CLOUDY with the metal ion fraction we are calculating set to unity. We assume solar abundances as was done in W09. We force hydrogen and helium to be fully ionised, resulting in  $n_e = 1.2n_{\text{H}}$  from these species alone. We then run CLOUDY again with the metal being calculated turned off, and difference the two sets of cooling efficiencies to obtain  $\Lambda'_{x_i}$ , which we tabulate for every metal ion in units of  $\text{erg cm}^3 \text{ s}^{-1}$ , because we divide out  $n_{x_i} n_e$  from the volumetric cooling rates to maintain density invariance. In practice the difference in  $n_e$  with the metal ion turned on and off is very small, since metal species do not contribute many electrons compared with H and He unless the metallicity is much higher than solar. The calculation for primordial ions is similar, except that the electron density will not default to  $n_e = 1.2n_{\text{H}}$  in the cases of H I, He I, and He II, because a significant fraction of the electrons can become bound. Therefore, we force  $n_e$  in our CLOUDY scripts to add in otherwise bound electrons for these primordial species, resulting in  $n_e = 1.2 \text{ cm}^{-3}$ . Our method differs from Gnat & Ferland (2012), who essentially make a single ion plasma to calculate cooling efficiencies. A strategy similar to ours was used to create the W09 tables except that W09 did not force ion states since its cooling was calculated assuming ionisation equilibrium.

The total summed net radiative cooling rate per unit volume of all species is

$$\Lambda_{\text{net}} = \sum_x \sum_i \Lambda_{\text{net},x_i} + \Lambda_{\text{Comp}}, \quad (7)$$

where inverse Compton cooling off the cosmic microwave background contribute  $\Lambda_{\text{Comp}} = 5.64 \times 10^{-36} \text{ erg K}^{-1} \text{ s}^{-1}$

<sup>5</sup> Further comparison figures are available on our website.

$(T - T_{\text{CMB},0} \times (1+z))(1+z)^4 n_e$ , using  $T_{\text{CMB},0} = 2.728$  K (Osterbrock & Ferland 2006).

The temperature evolution is calculated using

$$\frac{dT}{dt} = -\frac{\Lambda_{\text{net}}}{(3/2 + s)nk} + \frac{T}{\mu} \frac{d\mu}{dt}, \quad (8)$$

where  $n$ , the total number density of the gas, is  $\rho/(\mu m_{\text{H}})$  and  $\mu$ , the mean particle mass, is defined as

$$\mu = \frac{\rho}{nm_{\text{H}}} = \frac{\rho}{n_e + \sum_i n_{x_i}}, \quad (9)$$

where  $k$  is the Boltzmann constant, and  $s$  is 0 for isochoric (i.e. constant density) cooling and 1 for isobaric (i.e. constant pressure) cooling. The isobaric case cools more slowly owing to performing ‘‘PdV’’ work, and we refer the reader to §2.2 and §3 of GS07 for a more complete explanation of isochoric and isobaric cooling. We mainly focus on isochoric examples, because this is what is applicable to integrating cooling during a hydrodynamic timestep in a simulation. Lastly, the second term in Equation 8 accounts for the change in internal energy owing to the change in the number of particles sharing the internal energy in equipartition.

We define the cooling timescale as

$$\tau_{\text{cool}} = \frac{(3/2 + s)nkT}{\Lambda_{\text{net}}}. \quad (10)$$

and provide this timescale with data included on our website.

We will continue to update our ion-by-ion cooling data at our website <http://noneq.strw.leidenuniv.nl>. We note the recent improvements in atomic data used to calculate radiative cooling by Lykins et al. (2013). Our website will be updated to provide new cooling and ionisation coefficients from the most recently released official version of CLOUDY.

### 2.2.1 Cooling test cases

The top panel of Figure 3 shows the cooling functions ( $\Lambda'_{x_i}$ ) for individual oxygen ions and compares them to those of Gnat & Ferland (2012). We check that the two methods agree after scaling to CLOUDY default solar abundances.<sup>6</sup> The total volumetric cooling rate due to element  $x$  is  $\sum_i \Lambda'_{x_i} n_x n_e f_{x_i}$ . Our CIE oxygen ionisation fractions (solid lines) are compared to the CLOUDY fractions (dotted lines) in the second panel, demonstrating excellent agreement. The third panel shows the summed oxygen CIE cooling curve (thick black line) multiplied by  $n_e/n_{\text{H}}$  to plot cooling efficiency, combined with the contribution of each ion species (coloured lines). We compare this to the analogous CLOUDY calculation (grey solid line), which agrees almost perfectly above  $T = 10^4$  K and is virtually indistinguishable from our summed cooling curve. The cooling rate drops precipitously below  $T \sim 10^4$  K, because in CIE

$n_e$  declines steeply as hydrogen recombines. However, the CLOUDY calculation diverges and has much higher cooling owing to collisions other than electron-ion collisions, in this case H I-O I collisions. Our ion-by-ion cooling method fails in this regime for CIE, but we can still safely apply our method to photo-ionised cases below  $T = 10^4$  K where electron-ion collisions dominate cooling.

In the presence of a photo-ionisation background three things happen. First, ionisation removes electrons meaning higher ions exist at lower temperatures. This alone reduces cooling efficiencies in most cases, since higher ions usually have lower  $\Lambda'_{x_i}$  at a given temperature, because fewer radiative transitions exist; however there are exceptions. The fourth panel in Figure 3 shows the photo-ionisation equilibrium (PIE) ion fractions of oxygen for our code (solid lines) and the CLOUDY calculation (dotted lines). Here we use a density  $n_{\text{H}} = 10^{-4} \text{ cm}^{-3}$  and the HM01 EGB at  $z = 1$ . For states  $T \gtrsim 10^5$  K the agreement is excellent while there are some small, but noticeable deviations at lower temperatures for O III, O IV, and O V. The PIE cooling efficiencies in the bottom panel show very good agreement. Our investigation in Appendix A shows that low ions often agree less well with CLOUDY calculations than high ions.

Second,  $n_e$  does not decline at  $T < 10^4$  K, because photo-ionisation keeps most hydrogen ionised. Hence, for  $T < 10^4$  K the summed cooling of oxygen in the bottom panel (dashed thick black line) is actually much *higher* for PIE than for CIE owing to the much greater electron density. We provide tables down to  $T = 10^2$  K, because electron-ion collisions dominate the cooling in this regime given a realistic background.

Third, the total volumetric photo-heating of oxygen,  $\sum_i \epsilon_{x_i} n_x f_{x_i}$ , represented by the dotted thick black line in the bottom panel, adds energy to the gas. We do not show the contributions of individual species to the photo-heating as we do for the cooling. We plot net cooling, which is defined here as cooling minus heating, as the solid thick black line. For  $T < 10^4$  K even the net cooling due to oxygen is greater in PIE than in CIE! The point where cooling equals heating is  $10^{2.50}$  K for oxygen. However, the thermal equilibrium point for this entire solar abundance gas is at  $10^{4.23}$  K, mainly owing to hydrogen, and is indicated by the dashed vertical line in the bottom two panels. We compare to the CLOUDY values for cooling, heating, and net cooling with thick grey lines, finding very good agreement.

### 2.3 Cycling and sub-cycling

Given a timestep, which we will call the cycle timestep,  $dt$ , which may be the Courant timestep in a hydrodynamic code, we determine if the cooling rate needs to be updated on a shorter, sub-cycle timestep by determining if  $\delta u/u > \xi_{\text{cool}}$  where  $u$  is the internal energy density,  $\delta u \equiv \Lambda_{\text{net}} \times dt$  is the change in this energy, and  $\xi_{\text{cool}}$  is the fractional cooling tolerance. We then update the ionisation state explicitly on either the cycle timestep if  $\delta u/u \leq \xi_{\text{cool}}$ , or on the sub-cycle timestep defined by  $u/\Lambda_{\text{net}} \times \xi_{\text{cool}}$ . For the calculations presented here, we use  $\xi_{\text{cool}} = 0.01$ , but we find that running with 0.05 gives acceptable accuracy for much less computation time.

If we need to sub-cycle, we iterate cooling and ionisa-

<sup>6</sup> These abundances, also used in W09, are  $n_{\text{He}}/n_{\text{H}} = 0.1$ ,  $n_{\text{C}}/n_{\text{H}} = 10^{-3.61}$ ,  $n_{\text{N}}/n_{\text{H}} = 10^{-4.07}$ ,  $n_{\text{O}}/n_{\text{H}} = 10^{-3.31}$ ,  $n_{\text{Ne}}/n_{\text{H}} = 10^{-4.00}$ ,  $n_{\text{Mg}}/n_{\text{H}} = 10^{-4.46}$ ,  $n_{\text{Si}}/n_{\text{H}} = 10^{-4.46}$ ,  $n_{\text{S}}/n_{\text{H}} = 10^{-4.74}$ ,  $n_{\text{Ca}}/n_{\text{H}} = 10^{-5.64}$ , and  $n_{\text{Fe}}/n_{\text{H}} = 10^{-4.55}$ .



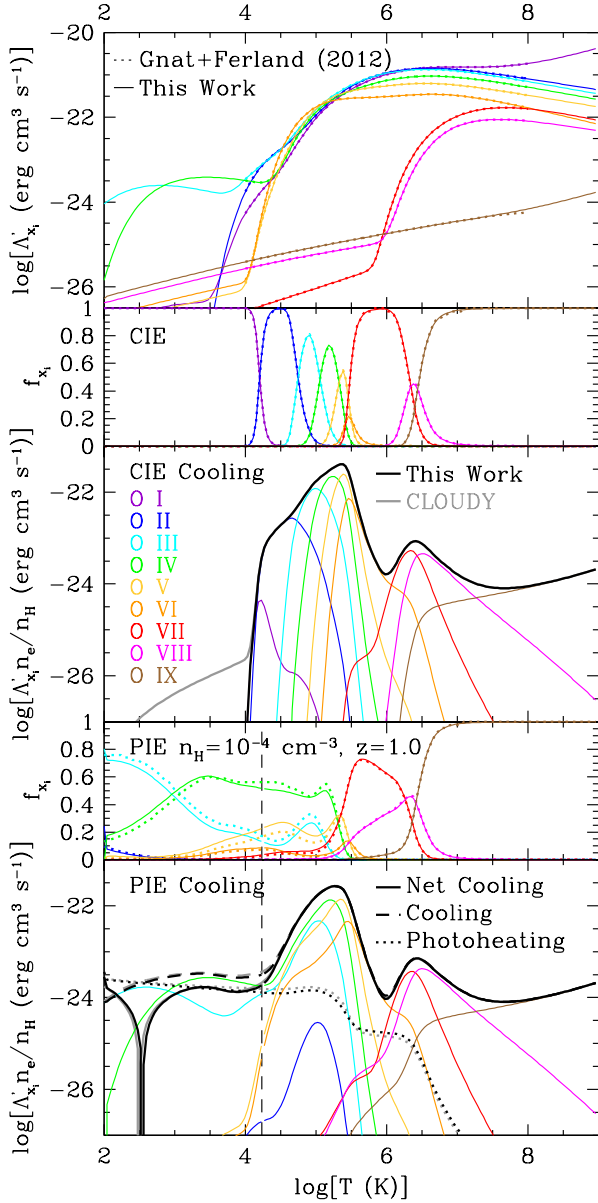


**Figure 3.** The top panel shows the cooling efficiencies of individual oxygen ions at solar abundance calculated by us using CLOUDY from  $T = 10^2 - 10^9$  K (solid lines) compared to efficiencies calculated by Gnat & Ferland (2012) using CLOUDY (dotted lines). The second panel compares the collisional ionisation equilibrium (CIE) oxygen fractions we calculate using our reaction network (solid lines) to those predicted by CLOUDY (dotted lines). The integrated oxygen CIE cooling efficiency, plotted as  $\Lambda'_{x_i} n_e / n_H$  (solid black line) in the third panel, is the sum of ion fractions multiplied by the ion cooling efficiencies (coloured lines), and agrees well with the CLOUDY case (grey line), except below  $T = 10^4$  K where our method loses accuracy due to the presence of cooling channels other than electron-ion collisions. The photo-ionisation equilibrium (PIE) oxygen ionisation fractions and summed cooling efficiency appear in the bottom two panels, assuming  $n_H = 10^{-4} \text{ cm}^{-3}$  and the HM01 EGB at  $z = 1$ . Cooling, photo-heating ( $\epsilon_{x_i} / n_H$ ), and net cooling ( $\Lambda_{\text{net}} / n_H^2$ ) are indicated in the bottom panel by dashed, dotted, and solid lines respectively for our code (black) and CLOUDY (grey). The equilibrium temperature of the solar abundance gas is indicated by the vertical dashed line.

tion, where the latter is integrated using CVODE as discussed in §2.1, explicitly until either i) the cycle timestep is reached, or ii) the equilibrium temperature is achieved by noting that the sign of  $\Lambda_{\text{net}}$  reverses. If a sign reversal occurs, we backtrack to the equilibrium temperature where  $\Lambda_{\text{net}} = 0$ , since further sub-cycling is unnecessary and computationally expensive. This is mainly a cosmetic choice as the internal energy will wiggle around the equilibrium temperature with a tolerance according to  $\xi_{\text{cool}}$  between cycles if the particle remains at the equilibrium temperature. The ionisation state will also wiggle, because the ionisation timescales are typically very short; hence our extra timestep attempts to prevent this unsightly wiggling.

Finally, it should be noted that the ionisation sub-cycle timestep is determined by cooling. The reverse, i.e. the cooling timestep being sub-cycled according to changes in the ionisation state, is not possible in our explicit method described thus far. In most cases applicable to diffuse gas, the cooling efficiency is not dramatically altered by a change in the ionisation state, but there are some notable exceptions. The most obvious example is reionisation, where the ionisation timescale is short and the cooling characteristics change dramatically from neutral to ionised. Another case is that of a nearby AGN suddenly turning on or off, changing the ionisation state on a timescale much shorter than the cooling time. We will explore the latter case in Oppenheimer & Schaye (in preparation), where we will also discuss how we address the sub-cycling. For now, we state that our current method is meant to follow cooling in the presence of a slowly changing EGB.

### 3 COLLISIONALLY IONISED NON-EQUILIBRIUM METAL-ENRICHED GASES

Before considering non-equilibrium ionisation in the presence of ionising radiation in §4, we will first consider only collisional processes and compare to previous results from GS07 (who used rates from CLOUDY ver. 06.02) and W09 (who used CLOUDY ver. 07.02). Figure 4 shows O VI (left panel) and O III (right panel) ion fractions as a function of temperature for cooling gas initially at  $T = 10^7$  K for the CIE and collisional non-equilibrium (CINe) cases at  $Z = 10^{-3}, 0.1, 1$ , and  $2 Z_{\odot}$ . Our calculations (solid lines) are compared to GS07 (dotted lines), who show the same two ions in their Figure 3. We have scaled our metal abundances to the abundances in their Table 1 for direct comparison. These calculations assume isochoric cooling, which is the default unless noted otherwise. We start in ionisation equilibrium at  $T = 10^7$  K, but the results are indistinguishable if the initial gas temperature is  $5 \times 10^6$  K as in GS07, because cooling times above this temperature are long and non-equilibrium ionisation is unimportant.

Figure 4 shows that the agreement with GS07 is good, and demonstrates the effects of non-equilibrium processes on ionisation fractions. Higher metallicities result in shorter cooling times and greater ionisation lags as recombination cannot catch up with cooling. Even for negligible metallicity,  $10^{-3} Z_{\odot}$  (cyan lines), which is so low as to not impact cooling times relative to primordial, there is non-equilibrium behaviour for O III (right panel). Primordial species have



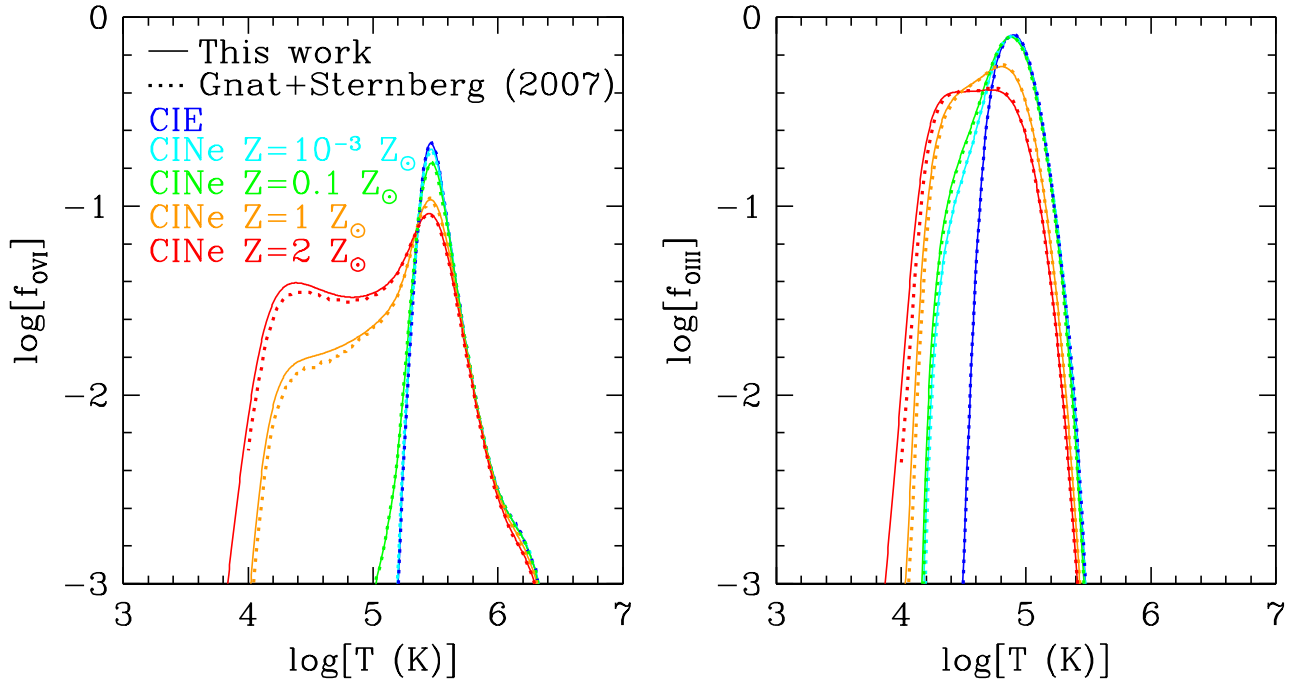


**Figure 4.** A comparison of the predicted ion fractions of O VI (left panel) and O III (right panel) as a function of temperature and computed assuming pure collisional ionisation (solid lines) with those of GS07 (dotted lines, see their Figure 3). The gas is assumed to cool isochorically, starting out in ionisation equilibrium at  $T = 10^7$  K. The collisional ionisation equilibrium case (blue) shows excellent agreement between the two methods, as do the non-equilibrium cases (other colours corresponding to different metallicities). Even for low metallicity,  $Z = 10^{-3} Z_{\odot}$  (cyan), non-equilibrium effects of primordial species cause O III ionisation fractions to diverge from CIE. Metal abundances have been scaled to the values assumed by GS07.

non-equilibrium ionisation lags, and GS07 demonstrated that this behaviour is independent of metallicity below  $\sim 10^{-2} Z_{\odot}$ . The main culprit is the ionisation lag of recombining hydrogen. Finally, it is worth noting that charge transfer is important for O III. Without recombination of O III owing to charge exchange, O III would persist at temperatures much below  $10^4$  K. The slight mismatches between our method and GS07 are likely due to the older atomic data used in CLOUDY ver. 06.02 by GS07.

Figure 5 shows the predicted isochoric cooling efficiencies (solid lines), plotted as  $\Lambda_{\text{net}}/(n_{\text{H}}n_{\text{e}})$  for CIE (blue for  $10^{-3} Z_{\odot}$ , magenta for  $Z_{\odot}$ ) and CINE (cyan for  $10^{-3} Z_{\odot}$ , orange for  $Z_{\odot}$ ). We compare to W09 (dashed lines) for the CIE cases, and to GS07 (dotted lines) in all cases. We use W09 solar abundances here and throughout the rest of the paper and note that the GS07 abundances are different. The differences with respect to GS07 for the cooling efficiencies at  $T \sim 10^5 - 10^6$  K is attributable to different neon abundances, which are nearly twice as high for GS07. The increased cooling at  $T > 10^6$  K for GS07 is due to updated atomic data between CLOUDY ver. 06.02 and ver. 10.00 (Gnat & Ferland 2012). These atomic updates were included in the CLOUDY ver. 07.02 used to generate the W09 tables, which show excellent agreement with our CIE cooling.

In CIE, the  $10^{-3} Z_{\odot}$  curves have peaks below  $10^5$  K corresponding to the collisional excitation of hydrogen

and helium, and a drop off at higher temperatures until Bremsstrahlung dominates above  $10^6$  K. Solar abundances increase cooling efficiencies by more than an order of magnitude between  $T \sim 2 \times 10^5$  and  $2 \times 10^6$  K. Below  $T = 10^4$  K, our method loses accuracy because cooling is no longer dominated by electron-ion collisions for this purely collisional example. The W09  $Z_{\odot}$  cooling efficiency jumps up, because ion collisions with neutral hydrogen dominate the cooling here. However, the cooling efficiency is much lower below  $T = 10^4$  K than the W09 magenta efficiency suggests, and the jump in the W09 rate is because we are dividing by  $n_{\text{e}}$  (to compare with GS07), which is very small. Hence, the cooling rate  $\Lambda_{\text{net}}$  is very small below  $10^4$  K both for W09 and us. Nevertheless, care should be taken when our method is applied to situations where cooling is not dominated by electron-ion collisions.

The CINE cases show the same characteristics as the corresponding GS07 efficiencies. In non-equilibrium the high ionisation fractions for primordial and metal species persist down to lower temperatures, where they are generally less efficient coolants. CINE cooling curves therefore are both smoother and lower than the corresponding CIE curves. This effect is also important for primordial species, which have very peaked CIE cooling efficiencies.

Below  $T = 10^4$  K, our method works for CINE cases as long as electron-ion interactions dominate the cooling, which is the case for solar metallicity. Vasiliev (2013) explore

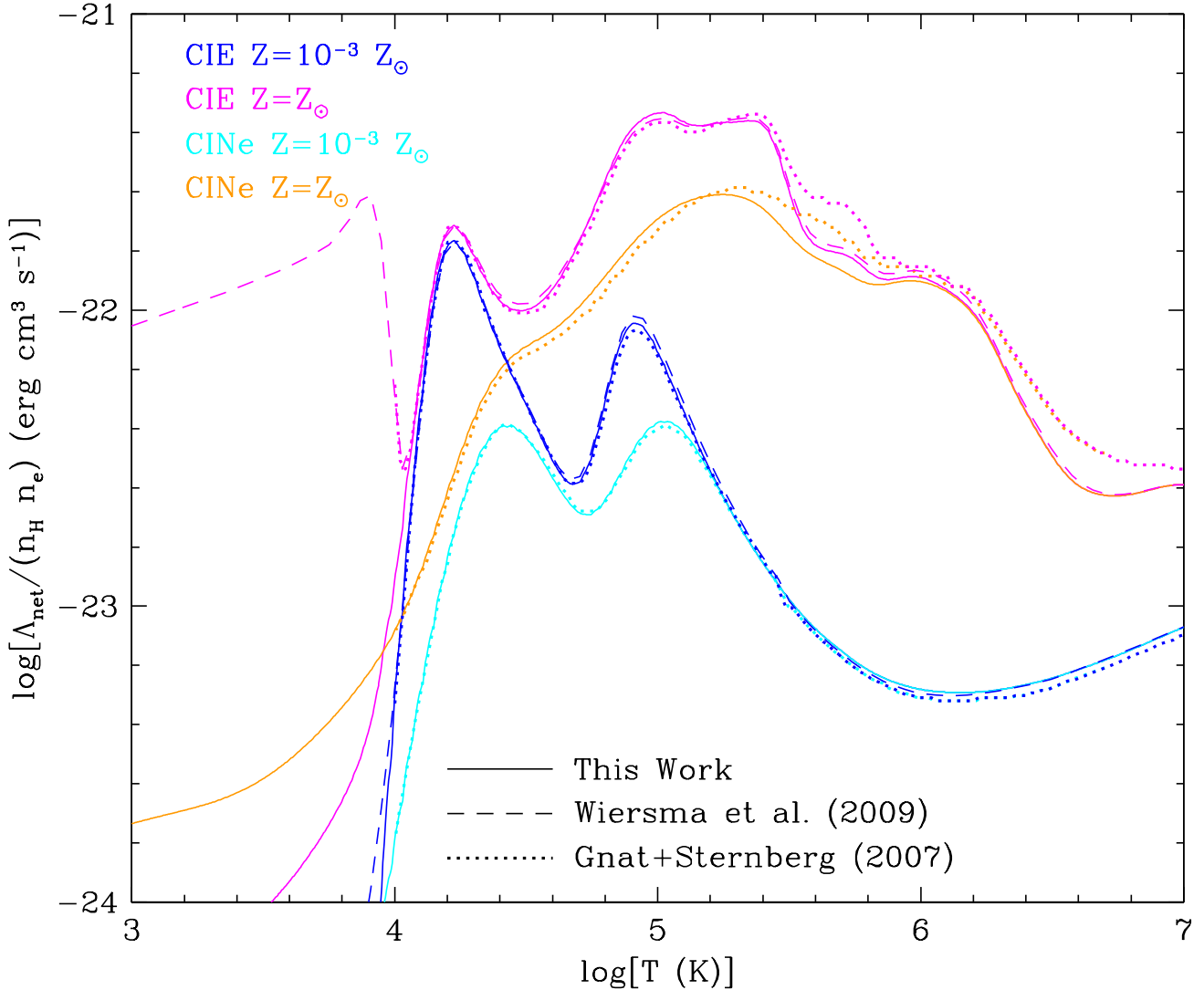


**Figure 5.** Isochoric cooling efficiencies (plotted as  $\Lambda_{\text{net}}/(n_{\text{H}}n_e)$ ) for collisional ionisation equilibrium (CIE) and collisional ionisation non-equilibrium (CINe) (solid lines) compared with W09 (dashed lines) and GS07 (dotted lines) for  $10^{-3} Z_{\odot}$  and  $Z_{\odot}$ . The agreement with W09 is excellent everywhere above  $10^4$  K. Comparison of our efficiencies to GS07 shows small deviations at higher temperatures partially owing to the different solar abundances used by GS07. We find the same non-equilibrium behaviour as GS07 of smoothed cooling curves as ion states persist down to lower temperatures where they generally are less efficient coolants. CINe curves begin in equilibrium at  $T = 10^7$  K, but CIE and CINe curves are indistinguishable at  $T > 10^6$  K.

CINe cases including molecules, finding that for  $Z \gtrsim 0.1 Z_{\odot}$  molecular cooling is negligible. Metals provide free electrons below  $T < 10^4$  K, which are far more efficient coolants than molecules or ion-ion interactions.

We compare the ionisation fractions for three collisional cases and solar metallicity in Figure 6: CIE Isochoric (solid lines), CINe Isochoric (dashed lines), and CINe Isobaric (dotted lines). For the isobaric case, we normalise the density to the isochoric cases at  $T = 10^6$  K. A variety of observationally obtainable metal ions are shown, starting with carbon species on top, oxygen species in the second panel, and silicon species combined with the Li-like ions N V, Ne VIII, and Mg X in the third panel. Our ion fractions compare well

with GS07 (their Figure 2), exhibiting the behaviour explained in their Figure 4. Briefly, He-like ions (C V, O VII) show the greatest ionisation lag, owing to having the longest recombination times. Isobaric cases do not have as great of an ionisation lag as isochoric cases, because of their longer cooling times at the same density due to extra “PdV” work. Our CIE ionisation fractions diverge from GS07 at  $T \sim 10^4$  K (cf. C II and Si II to their Figure 2) likely owing to ion-ion collisions, which are not included in our method, keeping the gas more ionised at  $T \lesssim 10^4$  K.

Finally, non-equilibrium effects are most important when cooling is most efficient, which is one reason we plot cooling times in the bottom panel. We use the specific case

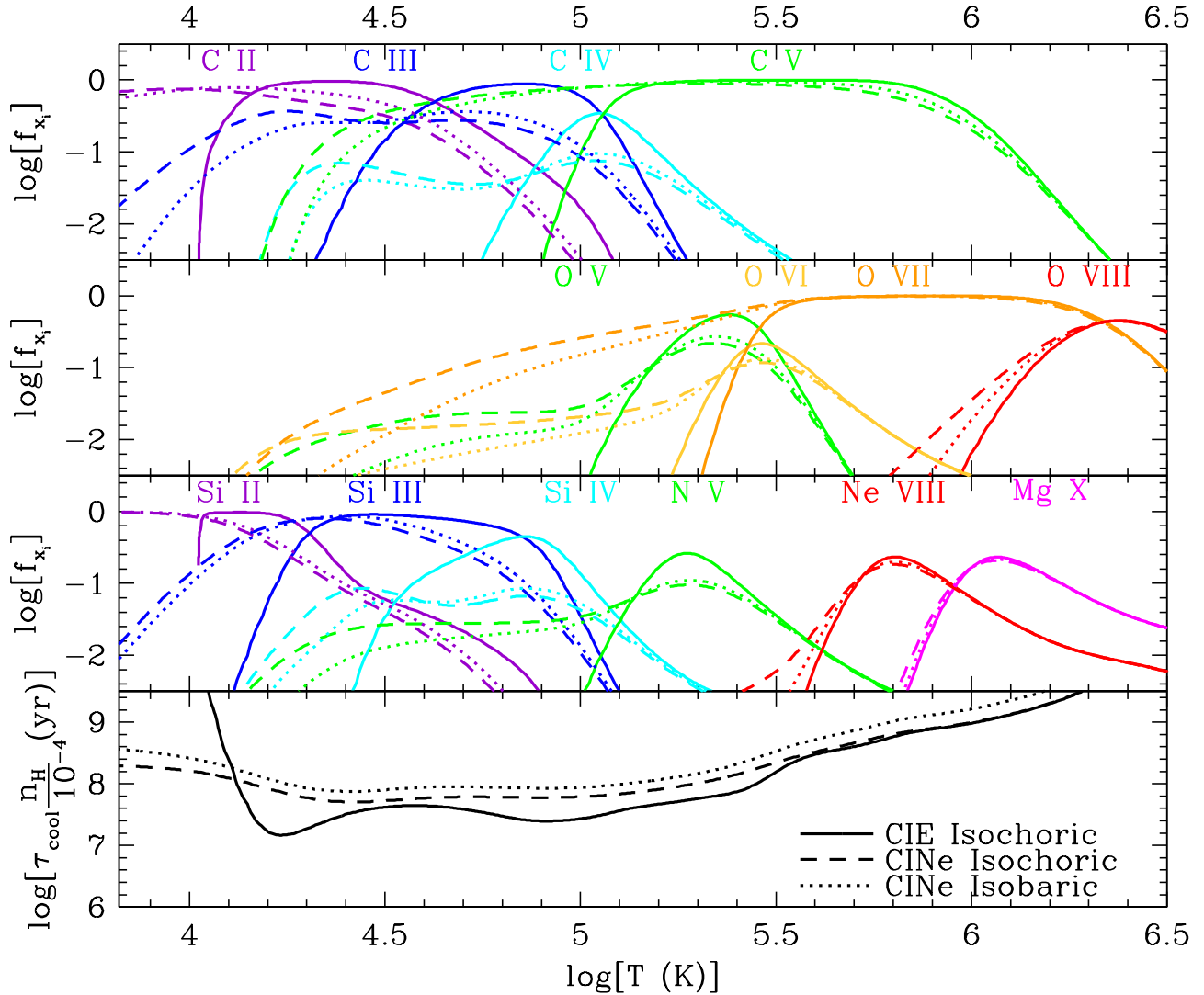


**Figure 6.** Collisional-only ionisation fractions for the same cases explored in GS07: collisional ionisation equilibrium (CIE Isochoric, solid lines), collisional ionisation non-equilibrium at constant density (CINE Isochoric, dashed lines) and at constant pressure (CINE Isobaric, dotted lines). We show ionisation fractions for some of the most common species observed in diffuse gas in the top three panels, as well as cooling times in the bottom panel to indicate how long cooling gas lives at each state, assuming a density of  $n_{\text{H}} = 10^{-4} \text{ cm}^{-3}$  and solar metallicity. The CINE Isobaric case matches the density of the CIE and CINE Isochoric cases at  $T = 10^6 \text{ K}$  (i.e.  $n_{\text{H}} = 10^{-4} \text{ cm}^{-3} (10^6 \text{ K})/T$ ). The CIE Isobaric case is not shown but would have the same ionisation fractions as the CIE Isochoric case while  $\tau_{\text{cool}}$  would be a factor 5/3 larger due to “PdV” work.

of  $n_{\text{H}} = 10^{-4} \text{ cm}^{-3}$  gas for comparison later with the photo-ionisation case in §4 that depends on the density in a non-trivial manner, but these cooling times scale inversely with  $n_{\text{H}}$ , which is why we plot  $\tau_{\text{cool}} n_{\text{H}} / (10^{-4} \text{ cm}^{-3})$ . For CINE, cooling is less efficient above  $1.3 \times 10^4$  but it is much more efficient at  $T < 10^4 \text{ K}$ , because  $n_e$  is much higher owing to H II persisting down to lower temperatures due to the recombination lag, and additionally H II is a more efficient coolant than H I at these temperatures. The CINE Isobaric case has density  $n_{\text{H}} = 10^{-4} \times (10^6 \text{ K}/T) \text{ cm}^{-3}$ , which means that for the same parcel of gas, the cooling will become faster at lower temperatures as its density rises. However, the cool-

ing efficiency ( $\text{erg cm}^3 \text{ s}^{-1}$ ) as plotted in Figure 5 is lower for the CINE Isobaric case compared to the CINE Isochoric below  $T = 10^4 \text{ K}$  owing to quicker recombination to metal ions that are less efficient coolants. This behaviour is also identified by Vasiliev (2013) (cf. their Figure 5 for  $Z_{\odot}$ ).

#### 4 PHOTO-IONISED NON-EQUILIBRIUM METAL-ENRICHED GASES

We now explore non-equilibrium processes in photo-ionised gases, which is the main innovation in this paper. Our motivation stems from the reality that metal-enriched diffuse

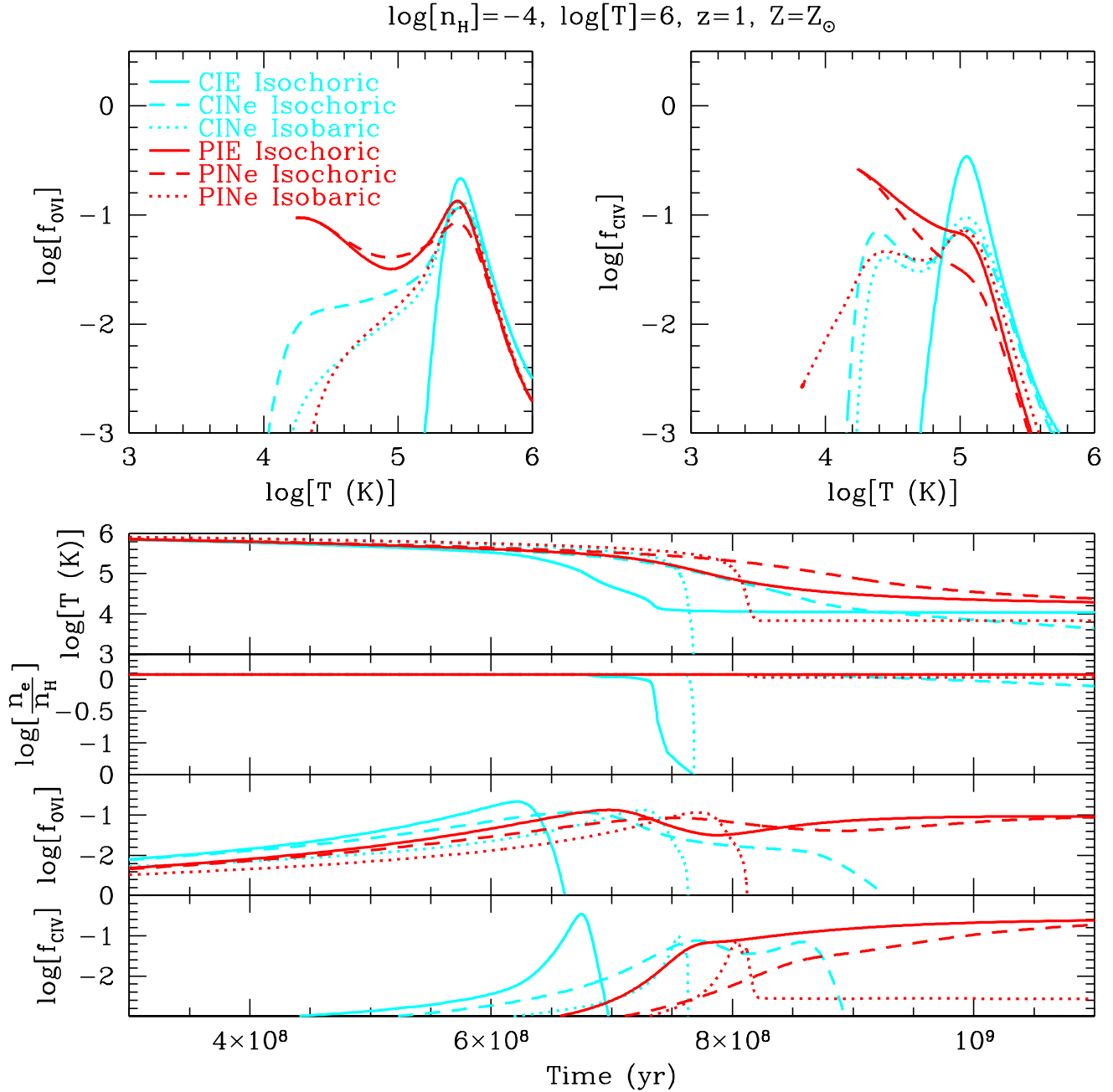


**Figure 7.** Ion fractions as a function of temperature for O VI (top left) and C IV (top right) for 6 cases at solar abundances: collisional ionisation equilibrium (CIE Isochoric, solid cyan), collisional non-equilibrium isochoric (CINE Isochoric, dashed cyan) and isobaric (CINE Isobaric, dotted cyan), photo-ionisation equilibrium (PIE Isochoric, solid red), photo-ionisation non-equilibrium isochoric (PINE Isochoric, dashed red) and isobaric (PINE Isobaric, dotted red). We also show the time evolution from  $T = 10^6$  K at  $t = 0$  yr in the bottom four panels of temperature, electron density, O VI and C IV fraction. We assume equilibrium initial conditions of  $n_{\text{H}} = 10^{-4} \text{ cm}^{-3}$  and  $T = 10^6$  K using the  $z = 1$  HM01 field in photo-ionised cases. All cases achieve  $T < 10^5$  K temperatures in under 1 Gyr with cooling trajectories, electron densities, and ionisation fractions as a function of time differing significantly.

gases cool in the presence of an ionising background, and that the cooling efficiencies, as well as the observational diagnostics, are altered by the addition of photo-ionisation to the non-equilibrium processes described in the previous section. The density-independence of collisional processes is broken, because the photo-ionisation rate per unit volume

due to a uniform field scales as  $n$ , while collisional processes scale as  $n^2$ . Our fiducial case is a  $n_{\text{H}} = 10^{-4} \text{ cm}^{-3}$ , solar abundance gas ionised by the HM01 EGB at  $z = 1$ . This corresponds to an overdensity,  $\delta \sim 60$ , and we will show that gas with this density cools in less than a Hubble time.

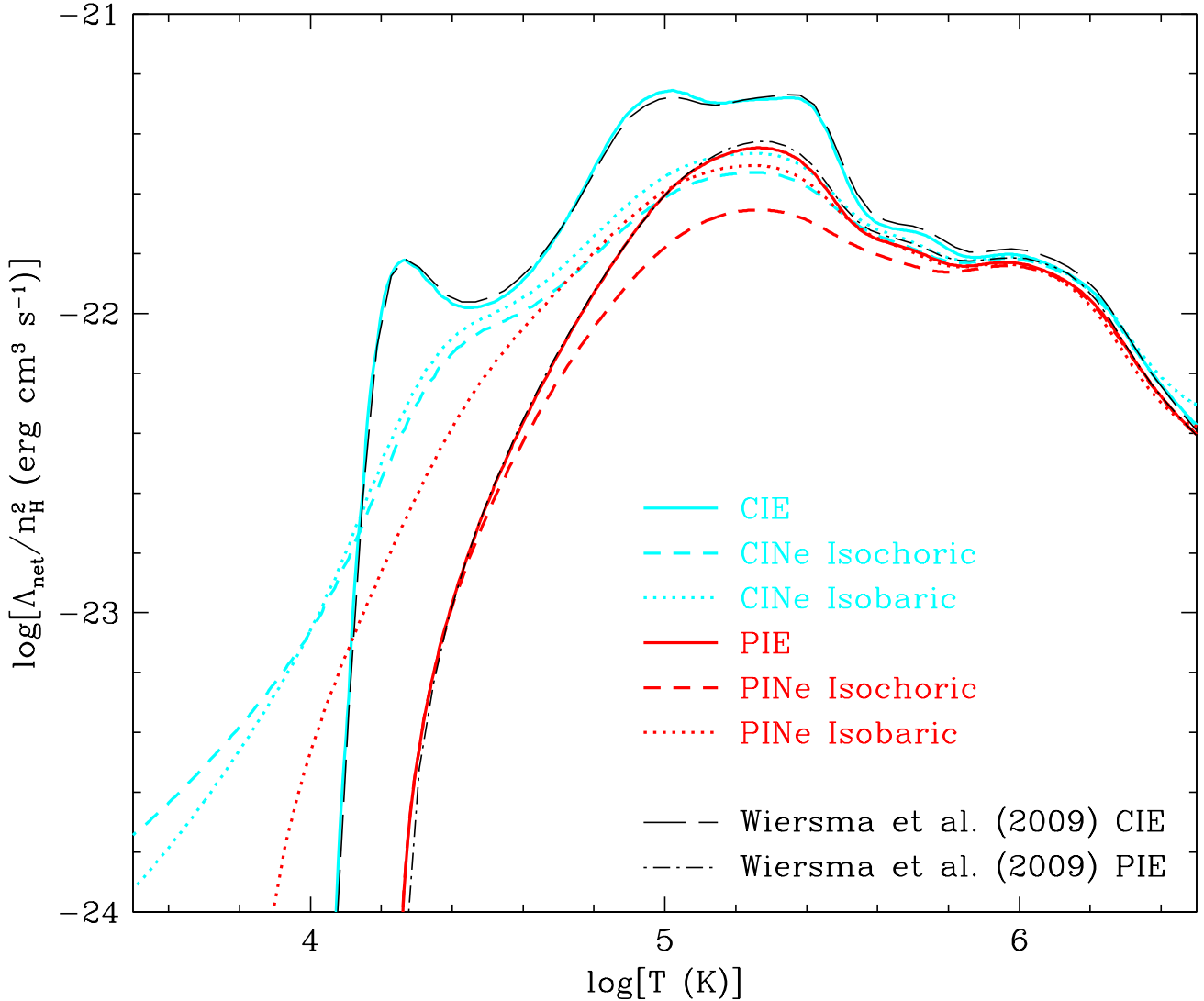


**Figure 8.** Cooling efficiencies, plotted as  $\Lambda_{\text{net}}/n_{\text{H}}^2$ , for the six cases displayed in Figure 7 assuming solar abundances at  $n_{\text{H}} = 10^{-4} \text{ cm}^{-3}$  and the HM01  $z = 1$  EGB. The isobaric cases are set to  $n_{\text{H}} = 10^{-4} \text{ cm}^{-3}$  at  $T = 10^6 \text{ K}$ . W09 cooling curves are displayed as thin dashed black lines for CIE and PIE at  $z = 0.957$ , and agree very well with our equilibrium models. Photo-ionisation suppresses cooling by removing bound electrons, most importantly from H I. Non-equilibrium effects at constant density suppress cooling owing to recombination lags where higher ions persist to lower temperatures where they are less efficient coolants. The isobaric cases follow the CINE Isochoric cases relatively closely, since the density dependence is divided out, although the PINE Isobaric case approaches an equilibrium temperature owing to photo-heating just below  $T = 10^4 \text{ K}$  and just above  $n_{\text{H}} = 10^{-2} \text{ cm}^{-3}$ . Non-equilibrium effects on cooling are smaller in the presence of ionising radiation, and the effect of photo-ionisation is smaller for isobaric than for isochoric cooling.

#### 4.1 Non-equilibrium behaviour

We consider the three cases explored in the previous section (CIE Isochoric, CINE Isochoric, and CINE Isobaric) along with three new situations with the added  $z = 1$  HM01 EGB: PIE Isochoric, photo-ionised non-equilibrium (PINE) Isochoric and PINE Isobaric. These six cases are shown in Figure 7. The gas begins in all cases in ionisation equilibrium at  $T = 10^6 \text{ K}$  and  $n_{\text{H}} = 10^{-4} \text{ cm}^{-3}$ . The top two panels show O VI and C IV fractions as functions of temperature. Below

this temperature, the cooling times become short enough to lead to non-equilibrium behaviour.

Comparing PIE to CIE, for PIE the O VI and C IV ion fractions are much higher below  $2 \times 10^5 \text{ K}$  and  $6 \times 10^4 \text{ K}$ , respectively, while these fractions are lower around the CIE peak. All photo-ionised curves asymptote to the equilibrium temperature where  $\Lambda_{\text{net}} = 0$ . Hence, if gas cools to the equilibrium point and stabilises (e.g. if  $\tau_{\text{dyn}} \gg \tau_{\text{cool}}$ ), then the gas will maintain the ionisation fractions corresponding to the equilibrium temperature.

Non-equilibrium effects in general allow ions to per-

sist to lower temperatures due to significant recombination times. For the PINE cases this effect is reduced as photo-ionisation also enhances the degree of ionisation in the equilibrium case. The impact of the photo-ionising background is smallest for the isobaric case because the density increases when cooling at constant pressure, thus decreasing the ionisation parameter.

The temperature evolution in the top of the lower panels of Figure 7 shows the unique thermal histories of gas in the six cases we explore. These behaviours are also reflected in the cooling curve plot in Figure 8 where we plot  $\Lambda_{\text{net}}/n_{\text{H}}^2$  to show net cooling efficiency for the six cases. We chose  $n_{\text{H}} = 10^{-4} \text{ cm}^{-3}$  at  $z = 1$  to show a case where photo-ionisation has a significant effect in gas that will cool in less than a Hubble time.

Photo-ionisation suppresses cooling relative to the collisional ionisation case whether in equilibrium or non-equilibrium. Considering the isochoric cases, non-equilibrium effects retard cooling compared to the equilibrium case resulting in the least efficient cooling curve of the six cases (Figure 8) and the hottest gas after the peak of the cooling efficiency ( $T < 10^5 \text{ K}$ ) at late times (Figure 7). The non-equilibrium suppression is greater for the collisional-only cases. Since the gas asymptotes to a highly ionised equilibrium state in the presence of ionising radiation, the non-equilibrium recombination lag affecting  $n_e$  and  $n_{\text{HI}}$  plays a smaller role and the cooling efficiencies of PIE and PINE Isochoric become nearly the same below  $T = 10^{4.5} \text{ K}$  (for  $n_{\text{H}} = 10^{-4} \text{ cm}^{-3}$  at  $z = 1$ ). Nonetheless, the reduced peak cooling rate of the photo-ionised cases delays the cooling of the gas by  $\sim 10^2 \text{ Myr}$  in this example. The isobaric non-equilibrium curves also show differences, but the effect of photo-ionisation is smaller, because these cases achieve higher densities at temperatures below  $T = 10^6 \text{ K}$  making photo-ionisation less important. The largest difference between the CINE and PINE isobaric cases is that the latter asymptotes to an equilibrium point after just 800 Myr when  $\Lambda_{\text{net}} = 0$ , which is achieved at a lower temperature,  $T = 10^{3.8} \text{ K}$ , for the isobaric density,  $n_{\text{H}} = 10^{-1.8} \text{ cm}^{-3}$ .

Figure 8 also shows that we reproduce the W09 PIE cooling curve very well with our ion-by-ion cooling scheme (cf. black thin dash-dot line and red solid line). We re-tabulated the PIE tables in the format of W09 using CLOUDY ver. 10.00 for both the Haardt & Madau (2001, 2012) backgrounds, and have posted them to our website <http://noneq.strw.leidenuniv.nl>.

Figure 9 shows the dependence of the PINE Isochoric evolution on the density. We scaled the time axes by  $n_{\text{H}}^{-1}$ , normalised to  $10^{-4} \text{ cm}^{-3}$ , to distill the effects of photo-ionisation on the temperature and ionisation. The CINE Isochoric case is shown in black for comparison. The effect of photo-ionisation is smallest at the highest densities. Lowering the density results in more delayed cooling even after removing the  $n_{\text{H}}^{-1}$  dependence of the cooling time, as well as higher equilibrium temperatures (i.e.  $\Lambda_{\text{net}} = 0$ ) because the photo-heating rate decreases less rapidly with the density than the cooling rate in this regime. The  $n_{\text{H}} = 10^{-5} \text{ cm}^{-3}$  case has the most extreme suppression of cooling shown, yielding a cooling time from  $10^6$  to  $10^5 \text{ K}$  of 19 Gyr, i.e. longer than a Hubble time. The EGB would therefore evolve, becoming weaker below  $z = 1$ , but we have turned off this evolution for simplicity. Finally, we note that Figure 9 also

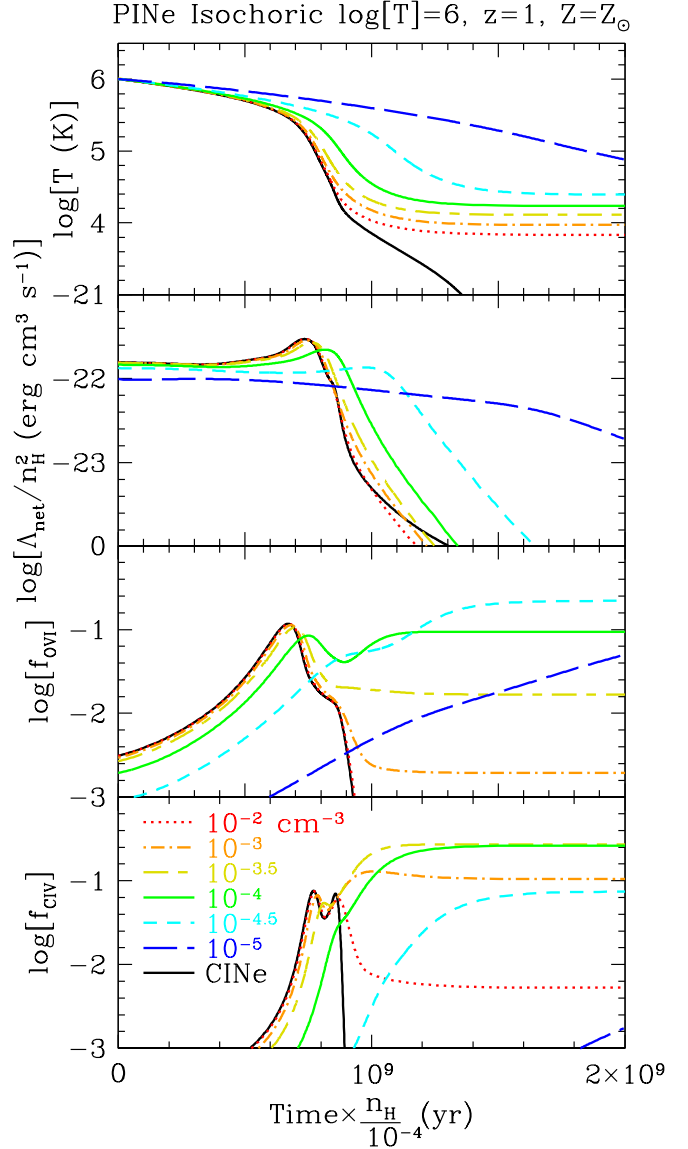


**Figure 9.** Evolution of non-equilibrium isochorically cooling solar abundance gas at various densities exposed to the  $z = 1$  HM01 radiation field (coloured lines) and assuming collisional ionisation only (solid black line). Ion fractions of O VI and C IV are shown along with the net cooling efficiency and temperature. The time axis is scaled by  $n_{\text{H}}$  and normalised to  $n_{\text{H}} = 10^{-4} \text{ cm}^{-3}$  to distill the effects of a uniform radiation field, which suppresses cooling more at lower densities. The PINE cases also illustrate the effect of turning up or down the HM01 field strength at  $n_{\text{H}} = 10^{-4} \text{ cm}^{-3}$ , e.g. the blue curve represents a  $10\times$  field increase and the red curve a  $100\times$  decrease.

shows the effect of adjusting the strength of the HM01 field by a factor of  $10^{-4} \text{ cm}^{-3}/n_{\text{H}}$  at fixed density if we keep the time axis fixed in absolute terms. For example, the blue  $n_{\text{H}} = 10^{-5} \text{ cm}^{-3}$  curve is applicable to a  $n_{\text{H}} = 10^{-4} \text{ cm}^{-3}$  gas cooling in a  $10\times$  stronger field and down to  $10^5 \text{ K}$  in 1.9 Gyr.

The ratios of isochoric cooling rates are displayed in Figure 10 as a function of density and temperature assum-



ing solar enriched gas irradiated by the  $z = 1$  HM01 EGB, initially at  $T = 10^7$  K. The relative cooling rates of PIE cooling versus CIE appear in the top panel, indicating that photo-ionisation suppresses the cooling rate more as the density goes down (or the ionisation parameter increases), as is demonstrated by W09. The bottom panel shows the ratio of PINE and PIE cooling rates to show where non-equilibrium effects become important for gas cooling dynamics. Non-equilibrium effects are more important at higher densities corresponding to circumgalactic halo gas, where photo-ionisation is weaker. At even higher densities than plotted here, the PINE/PIE cooling rate ratios reflect the CINE versus CIE case, as shown by Vasiliev (2011).

To summarise, photo-ionisation reduces cooling efficiencies and increases the degree of ionisation for both equilibrium and non-equilibrium cooling. Non-equilibrium effects on the evolution of the cooling rate and on the ionisation balance are smaller in the presence of ionising radiation. The effect of photo-ionisation is smaller for isobaric than for isochoric cooling, which also agrees with the conclusions of Vasiliev (2011).

#### 4.2 Metal-line diagnostics

QAL metal-line observations are used to diagnose both the physical state of the gas (e.g. its temperature, ionisation parameter, and chemical composition) and the dynamical state of the gas (e.g. radiative cooling, conductive interface, turbulent mixing layer, shock front). Calculations usually assume equilibrium ionisation or ignore the effect of photo-ionisation, which is why we emphasise the need to include both non-equilibrium and photo-ionisation in diagnosing metal lines.

The bottom two panels of Figure 7 demonstrate the evolution of the O VI and C IV ion fractions for our six fiducial cases and the bottom panels of Figure 9 show the evolution for different densities assuming PINE Isochoric cooling. Note that for radiatively cooling gas, the probability of observing the ion ratios at the peak of the cooling curve is small compared to the probability of observing the gas at either higher temperatures where cooling is slower, or at lower temperatures when the gas approaches thermal equilibrium when  $\Lambda_{\text{net}} = 0$ .

In Figure 11, we plot ion fractions for a variety of observed UV resonance transitions observed in QAL spectra for the PIE and PINE Isochoric cases for gas with  $n_{\text{H}} = 10^{-4} \text{ cm}^{-3}$  that is exposed to the  $z = 1$  EGB, as well as the CINE Isochoric case. Allowing for the presence of ionising radiation opens up a new set of solutions with this figure showing only one density for a specific EGB. Entirely new families of solutions are possible for varying densities and backgrounds, which is why we offer the ionisation fraction tables for several densities for the HM01 background at several redshifts on our website <http://noneq.strw.leidenuniv.nl>, and include the solutions also for the newer Haardt & Madau (2012) background. Additionally, we provide cooling efficiencies,  $\Lambda_{\text{net}}/n_{\text{H}}^2$ , and the  $\tau_{\text{cool}}$  as a function of temperature for various densities for the PIE Isochoric, PINE Isochoric, and PINE Isobaric cases.

Figures 7, 9, and 11 show that assuming CINE rather than PINE can easily lead to order of magnitude errors in the predicted ion fractions. An example of an application for

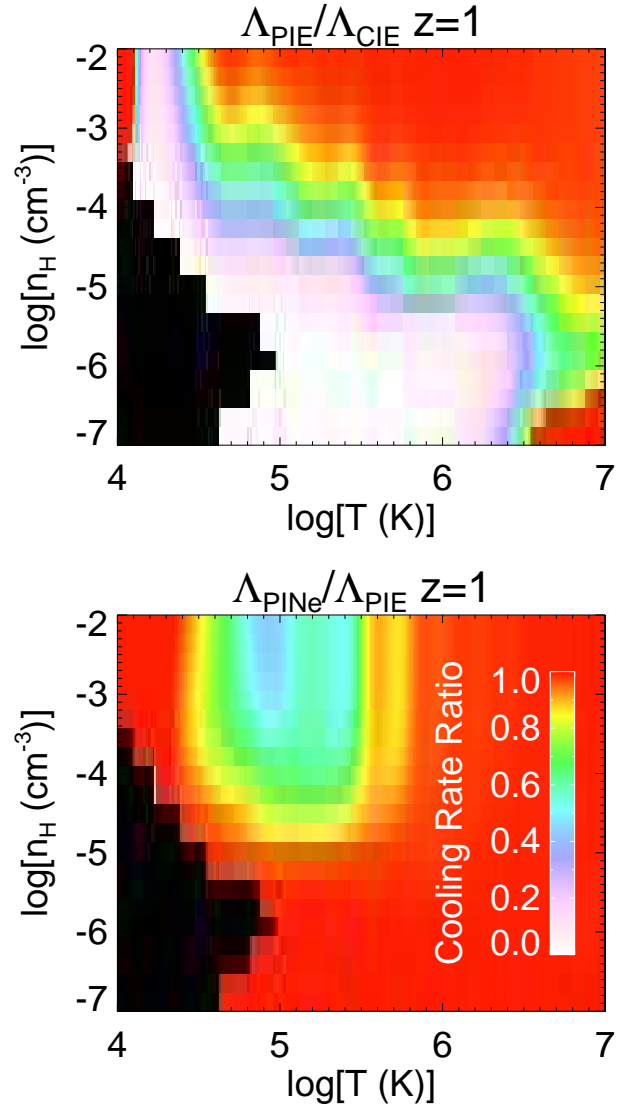


**Figure 10.** The ratio of net cooling rates as a function of temperature and density for  $Z = Z_{\odot}$  at  $z = 1$  assuming isochoric conditions beginning at  $T = 10^7$  K. The top panel shows the ratio of PIE to CIE cooling rates, indicating that photo-ionisation suppresses the cooling rate more at lower density (higher ionisation parameter). The bottom panel shows the ratio of PINE to PIE cooling rates, indicating that non-equilibrium processes affect cooling most at higher densities between  $T \sim 10^{4.5} - 10^6$  K. Cooling at high temperatures and low densities is dominated by Compton cooling, which has been subtracted here, but makes the comparison in the bottom right corner of the top panel inaccurate. Black corresponds to conditions where there is net heating.

which the difference is much smaller is a QAL component absorber with  $N_{\text{NeVIII}} \sim N_{\text{NV}}$ . This is very close to what has been observed by Tripp et al. (2011) who constrain the temperature of a radiatively cooling gas based primarily on these two species having similar columns (within 0.5 dex of each other) in various components of a single system. Since the solar number density abundances of nitrogen and neon are similar,  $N_{\text{NeVIII}} \sim N_{\text{NV}}$  means that  $f_{\text{NeVIII}} \sim f_{\text{NV}}$ . The rapid change in the N V and Ne VIII fractions as a function of temperature visible in the third panel of Figure 11 provides a powerful constraint for a single-phase radiatively cooling



gas model of  $T \sim 10^{5.5}$  K. By seeing where the respective green and red lines cross in this panel, we can see that photo-ionised models predict only slightly lower temperatures ( $T = 10^{5.46}$  K for PINE Isochoric) than for the collisional-only case ( $T = 10^{5.58}$  K). The ionisation correction also decreases for the PINE case as the ionisation fractions are 0.2 dex higher than for CINE meaning that taking photo-ionisation into account yields a lower gas mass.

However, we provide a cautionary note about applying a single-phase radiatively cooling solution to this situation, because the probability of catching gas cooling at a temperature where  $N_{\text{NeVIII}} \sim N_{\text{NV}}$  is low owing to  $\tau_{\text{cool}}$  being short (bottom panel of Figure 11). Gas at these temperatures can exist, but it is a priori much more probable to observe cooling gas at either lower temperatures where  $\tau_{\text{cool}}$  approaches infinity at the equilibrium temperature, or at  $T \gtrsim 10^6$  K where  $\tau_{\text{cool}}$  is longer. A multi-phase model comprising of radiatively cooling sub-clumps occupying a temperature distribution weighted by  $\tau_{\text{cool}}(T)$  between  $T \sim 10^4 - \gtrsim 10^6$  K is more conceivable. However, this model would fail likely owing to the hotter sub-clumps having significant Mg x absorption violating the upper limit constraint observed by Tripp et al. (2011). A related possibility is that metal-enriched gas has a maximum of  $T \sim 10^{5.5}$  K accompanied by a much larger reservoir at lower temperatures, which would not violate the Mg x upper limit. However, we provide an alternative model in Oppenheimer & Schaye (2013), which explains the observations by appealing to enhanced fossil photo-ionisation from a local AGN.

### 4.3 Ionisation background variations

Cooling efficiencies and QAL diagnostics both depend on the spectral shape and strength of the EGB. Thus far, we have used the HM01 EGB because it is widely used (e.g. Schaye et al. 2010; Oppenheimer et al. 2012) and because it fits observed metal ion ratios at  $z \sim 3$  (Aguirre et al. 2008), as well as the full H I column density distribution (Davé et al. 2010; Altay et al. 2011). However, the intensity and especially the shape of the EGB are rather uncertain as they depend on poorly constrained escape fractions, intrinsic spectral slopes, and extrapolations of luminosity functions. Recently published backgrounds include the Haardt & Madau (2012, hereafter HM12) and the Faucher-Giguère et al. (2009, hereafter FG11<sup>7</sup>) model. We plot these backgrounds at the output nearest to  $z = 1$  in the top panel of Figure 12 to demonstrate the variations in the EGB, especially at the extreme UV (EUV) energies that correspond to the ionisation potentials of commonly observed Lithium-like ions indicated in the Figure. The assumed QSO EUV slope ( $>13.6$  eV) ranges from  $\nu^{-1.5}$  to  $\nu^{-1.8}$  in the above listed models and can change the strength of the field by more than an order of magnitude at the ionisation energy of O VI (114 eV). Given that the observed QSO EUV slope ranges between at least  $\nu^{-3.0}$  and  $\nu^{0.0}$  (Telfer et al. 2002; Shull et al. 2012), we generate an EGB with a harder input QSO EUV slope,  $\nu^{-1.0}$ , using a post-2001, pre-2012 version of the CUBA package (F. Haardt, private communication).

<sup>7</sup> Using the Dec. 2011 update found at <https://www.cfa.harvard.edu/~cgiguere/UVB.html>

This background (H-1.0) is shown as the dotted blue line in Figure 12. This EGB may be relevant for diffuse metals in regions occupied by harder than normal QSOs.

Considering our fiducial case ( $n_{\text{H}} = 10^{-4} \text{ cm}^{-3}$  at  $z = 1$  and solar abundances), we show the PINE Isochoric cooling efficiencies for these four backgrounds in the middle panel of Figure 12. The cooling time from  $10^6 \rightarrow 10^5$  K, i.e. near the peak of the cooling curve, is 675 Myr for CIE and 773 Myr in CINE. The addition of photo-ionisation from the three published EGBs increases this cooling time to between 820 and 903 Myr. The more extreme H-1.0 EGB heavily suppresses metal coolants at these temperatures, increasing  $\tau_{\text{cool}}$  to 1.47 Gyr. Hence, the inclusion of non-equilibrium effects and photo-ionisation from a hard EGB can double the cooling timescale. Since the accretion of gas depends on its ability to cool, the process of galaxy formation can be significantly altered by photo-ionisation. This conclusion will only be strengthened if local sources of ionising radiation increase the intensity of the radiation field above that of the EGB. Such effects have been argued to be important (e.g. Schaye 2006; Cantalupo 2010; Rahmati et al. 2013), but we have conservatively ignored them here.

While the most extreme EGB reduces cooling efficiencies by a factor of two, the diagnostics of observed QAL can change much more as illustrated by the O VI fractions in the bottom panel of Figure 12. Below the peak of the CIE cooling curve (i.e. at  $T < 10^{5.3}$  K), O VI fractions are much higher for PINE than for either CIE or CINE. The difference between the different PINE cases is smaller ( $\approx 2\times$ ). We emphasise once again that, a priori, radiatively cooling gas is most likely to be observed when  $\tau_{\text{cool}}$  is longest, i.e. at the temperatures near the equilibrium point ( $T \sim 20,000 - 30,000$  K).

In a cooling rate ratio plot analogous to Figure 10, we vary the redshift of the HM01 EGB, while keeping  $n_{\text{H}} = 10^{-4.0} \text{ cm}^{-3}$  and assuming  $Z = Z_{\odot}$ . The top panel shows that PIE cooling is suppressed more than the CIE case at higher redshift, with the difference becoming less from  $z \sim 2 \rightarrow 0$  as the EGB weakens. The ratio of PINE to PIE cooling in the bottom panel shows that non-equilibrium cooling suppression is greatest at  $z = 0$  and  $z = 6$ , and reaches a minimum at  $z \sim 2.5$  when the background is strongest. A similar plot was made by Vasiliev (2011) (cf. their Figure 9), showing the same trend, but at a lower density ( $n = 10^{-4.0} \text{ cm}^{-3}$  or  $n_{\text{H}} \sim 10^{-4.3} \text{ cm}^{-3}$ ). In general, as the ionisation parameter increases, the cooling suppression owing to photo-ionisation becomes more important than the suppression owing to non-equilibrium effects.

## 5 SUMMARY

Radiative cooling is an essential ingredient for any model of the formation of galaxies and the evolution of the intergalactic medium. Cooling efficiencies depend on the chemical composition and the ionisation balance. Knowledge of the ionisation balance is also critical for the interpretation of observations of quasar absorption lines.

Although simulations nearly always assume ionisation equilibrium, this assumption will generally break down in gas that is cooling rapidly or that is exposed to a fluctuating radiation field. In particular, recombination lags may leave

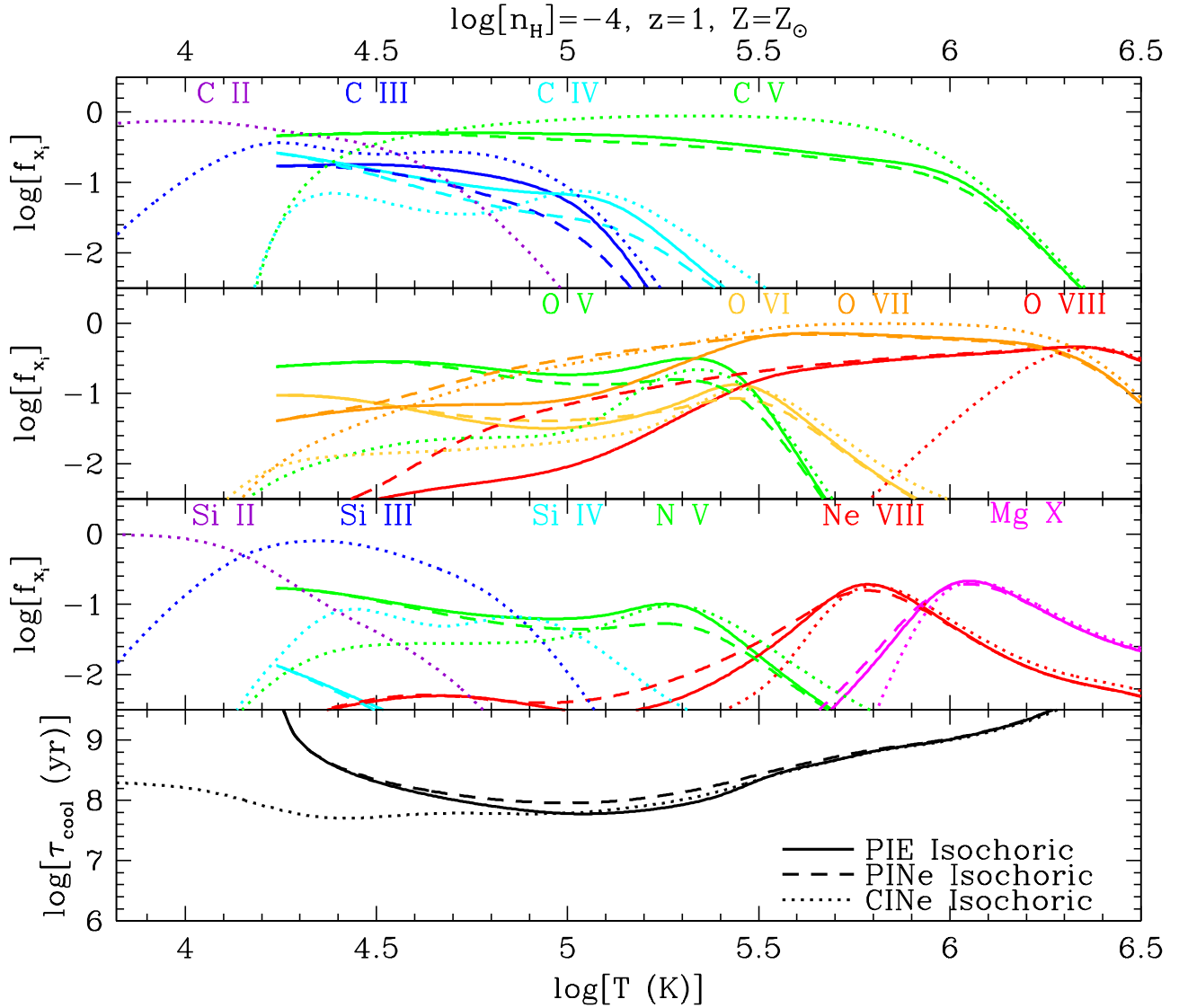


**Figure 11.** Ionisation fractions as a function of temperature for some of the most common species observed in isochoric, radiatively cooling diffuse gas along with cooling times (bottom panel) to indicate how long cooling gas lives at each state assuming  $n_{\text{H}} = 10^{-4} \text{ cm}^{-3}$ . We assume an initial temperature of  $T = 10^{6.5} \text{ K}$ . The density is fixed at  $n_{\text{H}} = 10^{-4} \text{ cm}^{-3}$  at all times. We assume solar abundances and, for the photo-ionised case (solid and dashed curves) the presence of the  $z = 1$  HM01 EGB. In contrast with the analogous plot for collisional-only ionisation (Figure 6 and dotted curves in this Figure), a given ionisation species will often persist to lower temperatures due to photo-ionisation and stop at  $T = 10^{4.1} \text{ K}$  owing to photo-heating balancing cooling. For isobaric cooling (not shown here) the differences between PINe and CINE are smaller than for isochoric cooling.

the gas over-ionised, thus reducing the cooling efficiency (e.g. Kafatos 1973; Gnat & Sternberg 2007).

Diffuse gas is exposed to the extra-galactic background radiation and possibly also to radiation from local sources. The presence of UV and X-ray radiation can strongly boost the ionisation of the gas and must therefore be taken into account when interpreting observations. The resulting removal of bound electrons injects energy (i.e. photo-heating), but also suppresses the cooling efficiencies of gas hot enough to cool through collisional excitation (Efstathiou 1992; Wiersma et al. 2009a, i.e.  $T > 10^4 \text{ K}$ ). Simulations

have only recently begun to take these effects into account for metals (e.g. Schaye et al. 2010; Ford et al. 2012), although still under the assumption of ionisation equilibrium.

Clearly, a realistic treatment of ionisation and cooling can neither assume ionisation equilibrium nor ignore the effects of the ionising background. In addition, the effects of non-equilibrium and photo-ionisation must be considered for both primordial and heavy elements.

We have presented a method for calculating non-equilibrium ionisation and cooling of diffuse gas exposed to ionising radiation. We consider 133 ionisation states of the

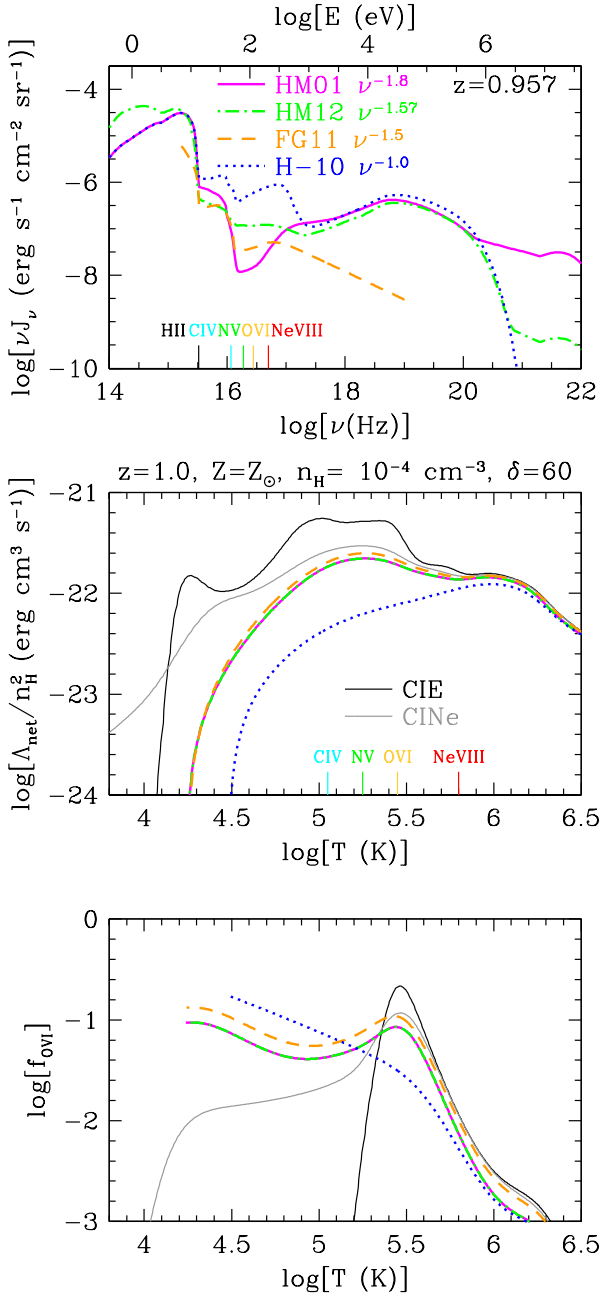


**Figure 12.** Demonstration of how different ionising backgrounds (top panel) affect radiative cooling efficiencies (middle panel) and ion fractions (OVI shown in bottom panel). Different versions of the EGB at  $z = 0.957$  show how changing the EUV slope can dramatically alter the ionising background at frequencies of commonly observed Lithium-like ion potentials. Non-equilibrium isochoric cooling curves for solar metallicity gas with density  $n_{\text{H}} = 10^{-4}$  cm<sup>-3</sup> beginning at  $T = 10^{6.5}$  K at  $z = 1$  (plotted as  $\Lambda_{\text{net}}/n_{\text{H}}^2$ ) show that harder radiation fields suppress cooling more by ionising metal coolants to a higher degree. For all backgrounds the cooling efficiency and OVI fraction are very different from the CIE and CINE cases (also shown in the bottom two panels).

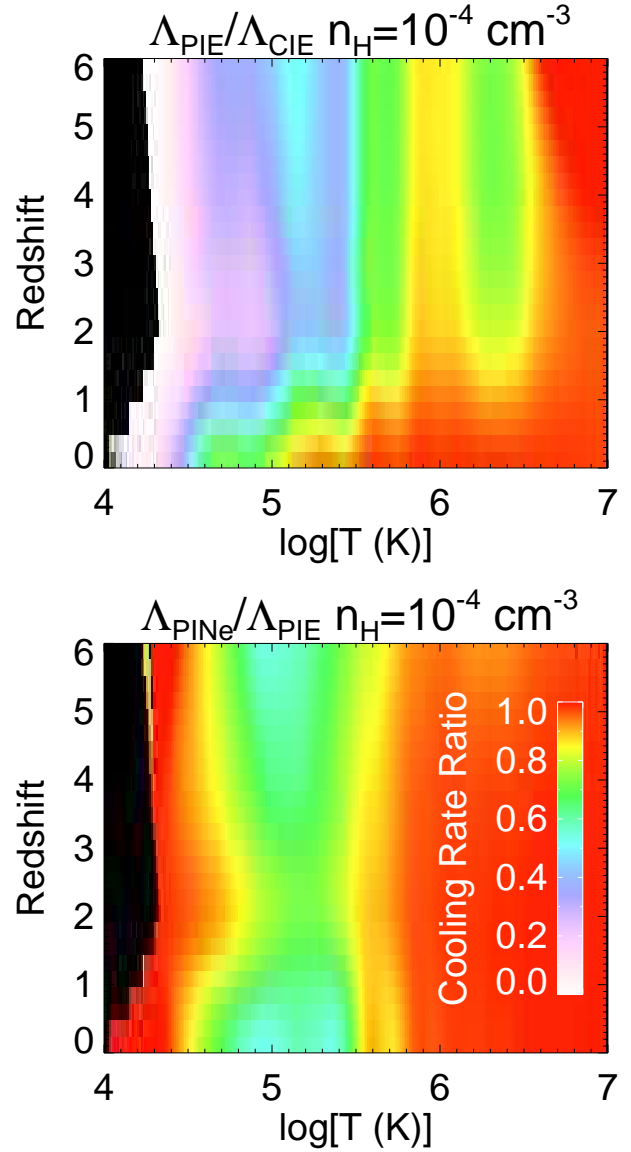


**Figure 13.** The ratio of net cooling rates as a function of temperature and redshift for  $Z = Z_\odot$  at  $n_{\text{H}} = 10^{-4.0}$  cm<sup>-3</sup> assuming the HM01 EGB. The top panel shows the ratio of PIE to CIE cooling rates, indicating that photo-ionisation suppresses more at higher redshift when the EGB is stronger. The bottom panel shows the ratio of PINE to PIE cooling rates, indicating that non-equilibrium processes affect cooling between  $T \sim 10^{4.5} - 10^6$  K at all redshifts, and the most when the EGB is weaker. Black corresponds to conditions where there is net heating.

11 species that dominate the cooling efficiencies of diffuse gas (H, He, C, N, O, Ne, Mg, Si, S, Ca, & Fe). Cooling and photo-heating efficiencies are computed ion-by-ion using tables generated with CLOUDY. After each time step, the ionisation balance is updated using a reaction network that includes radiative and di-electric recombination, collisional ionisation, photo-ionisation, Auger ionisation, and charge transfer. We make available the equilibrium and non-equilibrium calculations presented here in table format at <http://noneq.strw.leidenuniv.nl>. We also provide ionisation, recombination, cooling, and photo-heating coefficient input tables that can be integrated into hydrodynamic simula-

tions, and explain our method to use these in such calculations.

We demonstrated that our method reproduces published collisional ionisation equilibrium and non-equilibrium ionisation fractions and cooling efficiencies (Gnat & Sternberg 2007), and photo-ionised equilibrium ionisation fractions (Ferland et al. 1998) and cooling efficiencies (Wiersma et al. 2009a). We also reproduce the basic results of Vasiliev (2011), who also calculated non-equilibrium ionisation and cooling in the presence of an extra-galactic background (EGB).

Like Gnat & Sternberg (2007), we found that non-equilibrium cooling is confined to  $T < 10^{6.7}$  K. At these temperatures, the recombination time becomes significant compared to the cooling time, resulting in a recombination lag and reduced cooling efficiencies.

Photo-ionisation and non-equilibrium effects both tend to boost the degree of ionisation and to reduce cooling efficiencies, sometimes by significant factors. The effect of the EGB is larger for lower densities (i.e. higher ionisation parameters). Hence, photo-ionisation affects (equilibrium and non-equilibrium) cooling more under isochoric than under isobaric conditions. Non-equilibrium effects are smaller in the presence of an EGB and may therefore have been overestimated by previous work.

Observational diagnostics of diffuse, metal-enriched gases (e.g. metal absorption lines probed in quasar sight lines) are altered even more significantly than the cooling efficiencies, both under equilibrium and non-equilibrium conditions. Hence, the inclusion of the EGB opens up an entire new range of ionisation solutions depending on gas density, metallicity, and the strength and shape of the ionising radiation field.

We emphasised that not all ionisation solutions of a cooling gas should be treated with equal probability. For example, applying an ionisation solution to an observed absorption system that corresponds to a temperature near the peak of the cooling curve (i.e. where cooling times are shortest) assumes all the gas traced by the absorber has the solution that is a priori least probable. The addition of an EGB photo-heats the gas, usually leading to an equilibrium temperature where net cooling, radiative cooling minus photo-heating, is zero. Since the cooling time is effectively infinite at this point, this equilibrium solution with  $T \sim 10^4$  K, has a high probability.

Considering the dynamics of cooling is critical when applying a time-dependent solution to metal absorbers, which often require multi-phase models consisting of multiple parcels of gas at different temperatures. Hence, we provide dynamical cooling times and efficiencies with all the ionisation fractions included on our website. Our fiducial case of solar abundance gas at  $n_{\text{H}} = 10^{-4} \text{ cm}^{-3}$  irradiated by a  $z = 1$  EGB predicts much higher C IV and O VI fractions than pure collisional ionisation models.

We include coefficient lookup tables extending from  $T = 10^2 - 10^9$  K. Our method is applicable to cases when electron-ion collisions dominate the cooling, which includes nearly all intergalactic and circumgalactic gas. We demonstrate that our method works for metal-enriched gas at  $T < 10^4$  K that is ionised by the EGB. However our method is not accurate for  $T \leq 10^4$  K if H I is nearly fully neutral, e.g. in the dense parts of the interstellar medium, because

ion-ion interactions, molecules and dust may then be important.

We encourage the use of our website which provides photo-ionised, non-equilibrium ionisation and cooling data as a function of temperature for a larger range of redshifts, metallicities, and densities, including both the Haardt & Madau (2001) and (2012) backgrounds, than presented here. We will continue to update this website with the release of new versions of CLOUDY containing updated atomic data (e.g. Lykins et al. 2013). We also provide collisional and equilibrium results and provide some examples of how the calculations can be compared to observations.

Diagnosing the physical state of the metal-enriched intergalactic and circumgalactic media where cooling times are short requires tracking non-equilibrium ionisation in the presence of the ubiquitous extra-galactic background.

## ACKNOWLEDGEMENTS

We are grateful to Orly Gnat, Alex Richings, Chris Churchill, Kristian Finlator, Mike Shull, and Evgenii Vasiliev for stimulating discussions and assistance. We acknowledge Gary Ferland and the CLOUDY community for providing an essential tool in this work, and Francesco Haardt for providing the CUBA package to generate unique ionisation backgrounds. This work benefited from financial support from the Netherlands Organisation for Scientific Research (NWO) through VENI and VIDI grants, from NOVA, from the European Research Council under the European Unions Seventh Framework Programme (FP7/2007-2013) / ERC Grant agreement 278594-GasAroundGalaxies and from the Marie Curie Training Network CosmoComp (PITN-GA-2009-238356).

## REFERENCES

- Aguirre, A., Dow-Hygelund, C., Schaye, J., & Theuns, T. 2008, *ApJ*, 689, 851
- Aldrovandi, S. M. V., & Pequignot, D. 1973, *A&A*, 25, 137
- Altay, G., Theuns, T., Schaye, J., Crighton, N. H. M., & Dalla Vecchia, C. 2011, *ApJL*, 737, L37
- Arnaud, M., & Rothenflug, R. 1985, *A&AS*, 60, 425
- Badnell, N. R., O’Mullane, M. G., Summers, H. P., et al. 2003, *A&A*, 406, 1151
- Badnell, N. R. 2006, *ApJS*, 167, 334
- Bertone, S., Schaye, J., & Dolag, K. 2008, *Space Sci. Rev.*, 134, 295
- Bertone, S., Aguirre, A., & Schaye, J. 2013, *arXiv:1301.5330*
- Cantalupo, S. 2010, *MNRAS*, 403, L16
- Cen, R. & Fang, T. 2006, *ApJ*, 650, 573
- Cen, R., & Chisari, N. E. 2011, *ApJ*, 731, 11
- Choi, J.-H., & Nagamine, K. 2009, *MNRAS*, 393, 1595
- Davé, R., Oppenheimer, B. D., Katz, N., Kollmeier, J. A., & Weinberg, D. H. 2010, *MNRAS*, 408, 2051
- Dekel, A. & Birnboim, Y. 2006, *MNRAS*, 368, 2
- Efstathiou, G. 1992, *MNRAS*, 256, 43P
- Faucher-Giguère, C.-A., Lidz, A., Zaldarriaga, M., & Hernquist, L. 2009, *ApJ*, 703, 1416

- Ferland, G. J., Korista, K. T., Verner, D. A., Ferguson, J. W., Kingdon, J. B., & Verner, E. M. 1998, *PASP*, 110, 761
- Ford, A. B., Oppenheimer, B. D., Davé, R., et al. 2012, arXiv:1206.1859
- Fox, A. J., Savage, B. D., Wakker, B. P., et al. 2004, *ApJ*, 602, 738
- Fox, A. J., Ledoux, C., Petitjean, P., Srianand, R., & Guimarães, R. 2011, *A&A*, 534, A82
- Gnat, O. & Sternberg, A. 2007, *ApJS*, 168, 213
- Gnat, O. & Ferland, G. 2012, *ApJS*, 199, 20
- Haardt, F. & Madau, P. 1996, *ApJ*, 461, 20
- Haardt, F. & Madau, P. 2001, in “Clusters of galaxies and the high redshift universe observed in X-rays, Recent results of XMM-Newton and Chandra”, XXXVIth Rencontres de Moriond, eds. D.M. Neumann & J.T.T. Van.
- Haardt, F., & Madau, P. 2012, *ApJ*, 746, 125
- Haas, M. R., Schaye, J., Booth, C. M., et al. 2012, arXiv:1211.1021
- Kaastra, J. S., & Mewe, R. 1993, *A&AS*, 97, 443
- Kafatos, M. 1973, *ApJ*, 182, 433
- Katz, N., Weinberg, D. H., & Hernquist, L. 1996, *ApJS*, 105, 19
- Kereš, D., Katz, N., Weinberg, D. H., & Davé, R. 2005, *MNRAS*, 363, 2
- Kingdon, J. B., & Ferland, G. J. 1996, *ApJS*, 106, 205
- Lykins, M. L., Ferland, G. J., Porter, R. L., et al. 2013, *MNRAS*, 539
- Oppenheimer, B. D. & Davé, R. A. 2006, *MNRAS*, 373, 1265
- Oppenheimer, B. D. & Davé, R. A. 2009, *MNRAS*, 395, 1875
- Oppenheimer, B. D., Davé, R., Kereš, D., Fardal, M., Katz, N., Kollmeier, J., Weinberg, D. H. 2010, *MNRAS*, 406, 2325
- Oppenheimer, B. D., Davé, R., Katz, N., Kollmeier, J. A., & Weinberg, D. H. 2012, *MNRAS*, 420, 829
- Osterbrock, D. E., & Ferland, G. J. 2006, *Astrophysics of gaseous nebulae and active galactic nuclei*, 2nd. ed. by D.E. Osterbrock and G.J. Ferland. Sausalito, CA: University Science Books, 2006,
- Rahmati, A., Pawlik, A. H., Raičević, M., & Schaye, J. 2012, *MNRAS*, in press, arXiv:1210.7808
- Rahmati, A., Schaye, J., Pawlik, A. H., & Raičević, M. 2013, arXiv:1301.1978
- Savage, B. D., Lehner, N., Wakker, B. P., Sembach, K. R., & Tripp, T. M. 2005, *ApJ*, 626, 776
- Schaye, J. 2006, *ApJ*, 643, 59
- Schaye, J., et al. 2010, *MNRAS*, 402, 1536
- Schmutzler, T., & Tscharnuter, W. M. 1993, *A&A*, 273, 318
- Shapiro, P. R., & Moore, R. T. 1976, *ApJ*, 207, 460
- Shull, J. M., & van Steenberg, M. 1982, *ApJS*, 48, 95
- Shull, J. M., Roberts, D., Giroux, M. L., Penton, S. V., & Fardal, M. A. 1999, *AJ*, 118, 1450
- Shull, J. M., Stevans, M., & Danforth, C. W. 2012, *ApJ*, 752, 162
- Smith, B. D., Hallman, E. J., Shull, J. M., & O’Shea, B. W. 2011, *ApJ*, 731, 6
- Springel, V. 2005, *MNRAS*, 364, 1105
- Sutherland, R. S., & Dopita, M. A. 1993, *ApJS*, 88, 253
- Telfer, R. C., Kriss, G. A., Zheng, W., Davidsen, A. F., & Tytler, D. 2002, *ApJ*, 579, 500
- Tepper-Garcia, T., Richter, P., Schaye, J., Booth, C. M., Dalla Vecchia, C., Theuns, T., & Wiersma, R. P. C. 2011, *MNRAS*, accepted
- Tripp, T. M., Meiring, J. D., Prochaska, J. X., et al. 2011, *Science*, 334, 952
- van de Voort, F., Schaye, J., Booth, C. M., Haas, M. R., & Dalla Vecchia, C. 2011, *MNRAS*, 414, 2458
- van de Voort, F., Schaye, J., Altay, G., & Theuns, T. 2012, *MNRAS*, 421, 2809
- Vasiliev, E. O. 2011, *MNRAS*, 414, 3145
- Vasiliev, E. O. 2013, arXiv:1302.0159
- Verner, D. A., & Yakovlev, D. G. 1995, *A&AS*, 109, 125
- Verner, D. A., Ferland, G. J., Korista, K. T., & Yakovlev, D. G. 1996, *ApJ*, 465, 487
- Verner, D. A., & Ferland, G. J. 1996, *ApJS*, 103, 467
- Voronov, G. S. 1997, *Atomic Data and Nuclear Data Tables*, 65, 1
- Wiersma, R. P. C., Schaye, J., & Smith, B. D. 2009, *MNRAS*, 393, 99
- Yoshikawa, K., & Sasaki, S. 2006, *PASJ*, 58, 641

## APPENDIX A: EQUILIBRIUM IONISATION COMPARISONS WITH CLOUDY

We compare equilibrium ionisation fractions calculated using our method assuming a  $z = 1$  HM01 background to those of CLOUDY ver. 10.00 for a range of diffuse gas densities and temperatures in Figure A1. Red and black contours indicate ion fractions for our method and CLOUDY, respectively. Black contours overlap red contours in most cases, indicating excellent agreement. The shading indicates the ratio  $\log[f_{\text{ThisWork}}/f_{\text{CLOUDY}}]$  where either ion fraction is  $> 10^{-3}$  if a metal ion or  $> 10^{-8}$  if H or He; green indicates a good fit, while purple (orange) indicates our method yields too low (high)  $f_{x_i}$  compared to CLOUDY. Note that our shading is very sensitive to differences between the two methods in order to highlight slight inconsistencies, and often the contours nearly overlap when shading is off-green.

For primordial species, the two methods agree well, except for H I at  $T \approx 15,000$  K and  $n_{\text{H}} > 0.1 \text{ cm}^{-3}$  where collisional ionisation causes a rapid transition in temperature between neutral and highly ionised. We assume case A recombination in our method aimed to track diffuse ionised gases, and case B recombination is more applicable when the gas is optically thick to Lyman series photons. Nonetheless the two sets of contours still nearly overlap.

O VII and Ne VIII show excellent agreement, except at higher photo-ionised densities where  $f_{x_i}$  drops off rapidly with increasing density. This is also apparent in Figure 2 and is of little practical concern. C IV also shows excellent agreement, although slight deviations occur where collisions dominate below  $T = 10^5$  K, which is also of little concern since  $f_{\text{CIV}}$  is very low here. Mg II shows good agreement, but reflects the disagreement with H I at the same range of densities around  $T = 15,000$  K, owing to spurious H I and electron densities. Again, the contours show excellent agreement. The bottom three panels of Figure A1 show a selection of some of the worst agreeing species, which likely owe to more complex treatment of radiative and dielectronic recombination in CLOUDY ver. 10.00. These species are also less

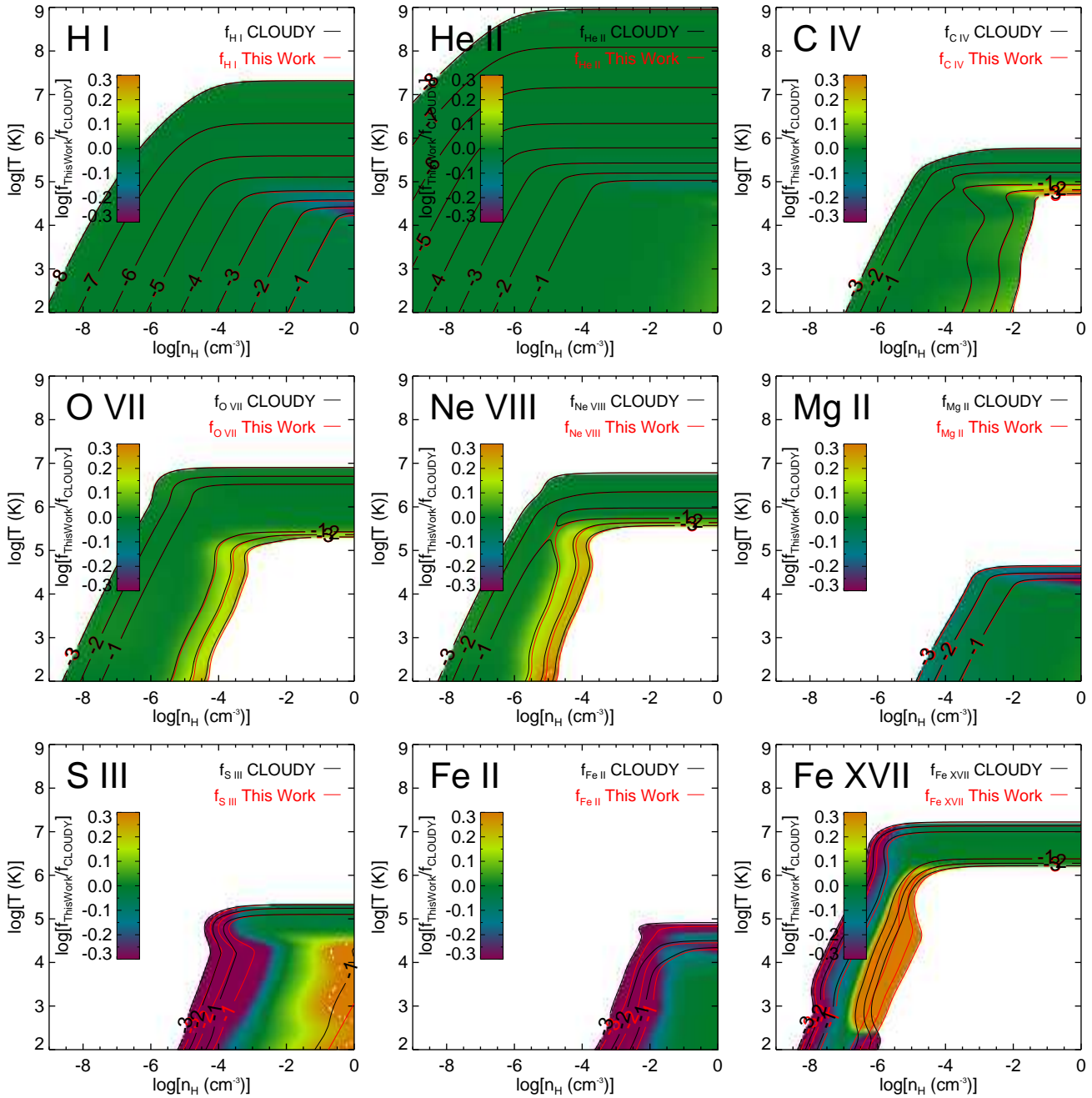


**Figure A1.** A selection of equilibrium abundances of common ions compared between our method (red contours) and CLOUDY (black contours). The colour bar shows the ratio of the ion fractions predicted by the two methods. In both cases, we turn on Auger ionisation and charge transfer. In general the agreement is very good as can be seen by comparing the black and red contours, although differences are highlighted by the very sensitive colour scaling that we choose. Where photo-ionisation is dominant for H I and He II, the agreement is excellent, but small differences occur in the regime where collisional ionisation dominates and H I becomes primarily neutral; this has to do with our assumption of case A recombination, which breaks down in this regime. In general, Li-like and He-like ions (C IV, O VII, and Ne VIII) show good agreement although slight differences can exist at higher photo-ionised densities where  $f_{x_i}$  drops off precipitously with increasing density. Mg II shows good agreement except where H I fractions are underestimated, and the electron density is thus different between the two cases, which affects low ions like Mg II in the regime where collisional ionisation becomes important. We also show some species in the bottom row that are more spurious, likely owing to a more complex set of radiative and dielectronic recombination coefficients used in CLOUDY (S III, Fe II, and Fe XVII).

studied in laboratory experiments and the relevant atomic data is therefore often less well constrained. The excellent agreement we demonstrate between cooling efficiencies calculated by CLOUDY and us indicates that these ion abundance differences are not important for the dynamics of gas, but they may be important for the diagnostics of the gas if these particular species are observed. Comparisons with CLOUDY for additional ions can be found on the website <http://noneq.strw.leidenuniv.nl>.

In Figure A2 we demonstrate the effect of Auger ionisation on O VI at  $z = 1$ . In the left panel we have Auger turned off both in CLOUDY and our method; the centre panel has Auger turned on in CLOUDY only; and the right panel shows it turned on in both. In the case of oxygen, photo-ionisation of the 1s shell of O I through O V leads most often to the removal of two electrons, which is why O VI is more ionised with Auger ionisation turned on, especially at photo-ionised temperatures at densities above the peak of the photo-ionised O VI fraction. Hence, Auger ionisation is important for O VI strengths at these densities and temperatures, and would be about  $2\times$  lower if Auger ionisation is ignored.

We perform an analogous comparison for O I and the effect of charge transfer (CT) in Figure A3 as we did for O VI and the Auger effect in Figure A2: from left to right the panels show no CT in either case, CT only in CLOUDY, and CT in both. If CT is not turned on, the O I fraction is underestimated by an order of magnitude at temperatures where it is found. O I shows extreme sensitivity to charge transfer owing to O I having a very similar ionisation potential as H I.



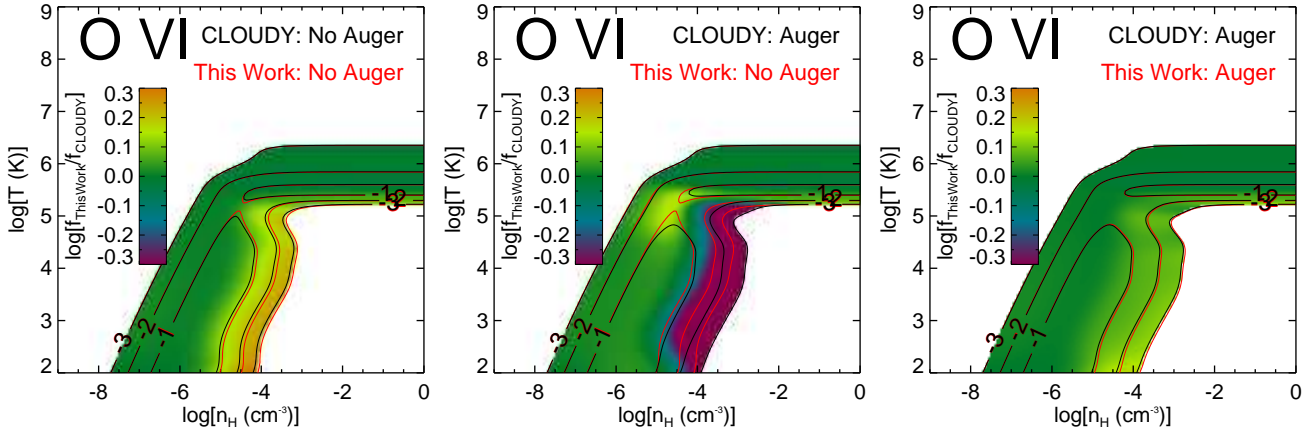


**Figure A2.** Comparison of O VI fractions predicted using our method calculated in equilibrium (red contours) and CLOUDY (black contours). Contours correspond to logarithmic ionisation fractions, and colour shading indicates the ratio of our method’s ionisation fraction over that of CLOUDY, according to the logarithmic colour bar. From left to right, we show the O VI fractions without Auger ionisation in either case (left), with Auger ionisation on for CLOUDY only (centre), and with Auger ionisation on in both methods (right). Auger ionisation boosts the O VI fraction at photo-ionised temperatures at the high density end.

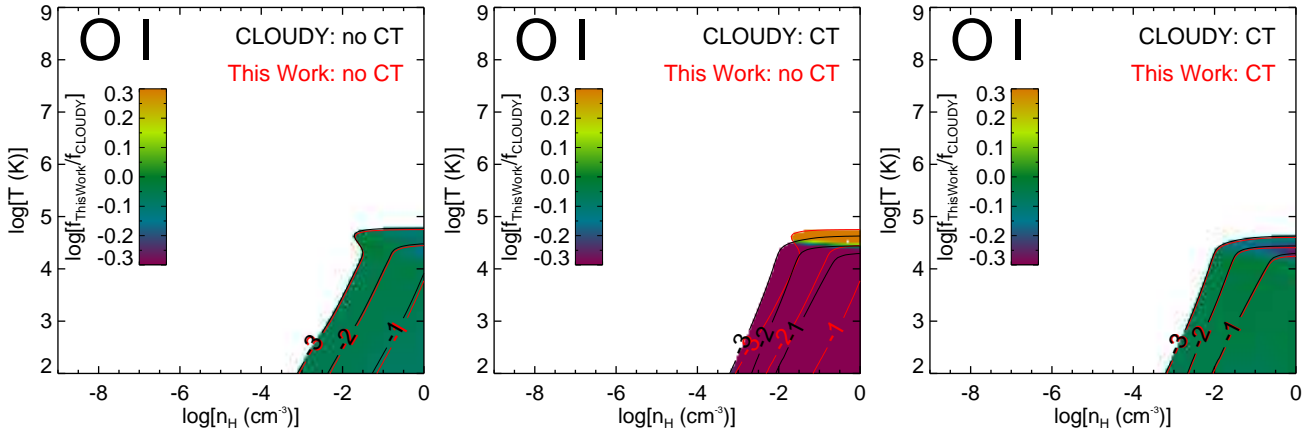


**Figure A3.** A similar plot as Figure A2, but for O I and the effect of charge exchange. Red contours indicate our ionisation fractions, and black contours indicate CLOUDY results. From left to right, we show the O I fractions without charge transfer in either case (left), with charge transfer on for CLOUDY only (centre), and with charge transfer on in both cases (right). Charge transfer is very important for O I owing to its similar ionisation potential with H I, and it is also significant for many of the other lower ions.